INSTITUTE OF FLUID-FLOW MACHINERY
POLISH ACADEMY OF SCIENCES

TRANSACTIONS OF THE INSTITUTE OF FLUID-FLOW MACHINERY

142

GDAŃSK 2023

TRANSACTIONS OF THE INSTITUTE OF FLUID-FLOW MACHINERY Appears since 1960

Aims and Sope

Transactions of the Institute of Fluid-Flow Machinery have primarily been established to publish papers from disciplines represented at the Institute of Fluid-Flow Machinery, Polish Academy of Sciences, such as:

- Renewable energy sources and distributed energy generation
- Hydrodynamics and hydraulic machinery
- Fluid mechanics with heat transport, particularly two-phase flows
- Various aspects of plasma and laser engineering development,
- Solid mechanics, mechanics of machinery
- Performance, monitoring and diagnostics problems in fluid-flow machinery

The journal originally used for publication of papers describing the research conducted at the Institute has now appeared to be the place for publication by authors both from Poland and abroad. A traditional scope of topics has been preserved.

Only original papers submitted in English version, representing both theoretical and applied sciences are published. All papers are reviewed by two independent referees.

EDITORIAL BOARD

SECTION EDITORS

EDITORIAL AND PUBLISHING OFFICE

Wydawnictwa IMP (IMP Publishers), Institute of Fluid-Flow Machinery,
ul. Fiszera 14, 80-231 Gdańsk, Poland, Tel.: (+48) 58-52-25-141, Fax (+48) 58-341-61-44,
E-mail: redakcja@imp.gda.pl, jfrk@imp.gda.pl, https://www.imp.gda.pl/transactions-of-iffn

Typeset in LaTeX

Articles in ***Transactions of the Institute of Fluid-Flow Machinery*** **are abstracted and indexed within:**

Index Copernicus
Google Scholar
Energy Citations Database
Applied Mechanics Reviews
BazTech
http://yadda.icm.edu.pl/baztech/element/bwmeta1.element.baztech-journal-0079-3205-transactions_of_the_institute_of_fluid-flow_machinery

ISSN 0079-3205

Thermal and morphological studies of additively manufactured CFRP composites under thermal loadings

Isyna Izzal Muna *

Institute of Fluid-Flow Machinery, Polish Academy of Sciences
14 Fiszera Street, 80-231, Gdansk, Poland

Abstract

The aim of this experimental work is to study the thermal and morphological properties of carbon fiber reinforced polymer (CFRP) as polymeric composites printed using additive manufacturing via material extrusion. The printed samples were exposed to prolonged temperatures at 65°C, 145°C, 0°C and -20°C. Differential Scanning Calorimetry (DSC) was performed to analyze the thermal properties of CFRP composites and the scanning electron microscope (SEM) was utilized to study the morphological structure of the sample groups after thermal treatment. The specimens subjected to cyclic heating at hot temperatures have higher glass transition temperature (Tg) values than the prolonged groups. The visual examination of the morphological structure at the surface showed a slight deterioration in the morphological surface before and after thermal treatment at above-zero degrees Celcius. The higher the magnitude of the temperature treatment at above-zero degrees, the more damage is possessed in the polymer parts.

Keywords: CFRP composites; additive manufacturing; thermal characterization; morphological characterization; thermal treatment

1 Introduction

Carbon fiber reinforced polymeric (CFRP) composites are widely used in aerospace structures (tails, wings, fuselages), wind turbine blades, and marine engineering (boat construction) applications where structures must be lightweight, have exceptional mechanical strength, and withstand extreme environmental conditions. Rapid advancements in manufacturing techniques and the design of new materials and structures in the engineering sector have piqued the interest of industry and scientific research.

Additive manufacturing (AM) or three-dimensional (3D) printing, is a set of manufacturing techniques that allows for the layer-by-layer production of 3D components with complex geometries. Complex composite structures that are difficult to fabricate using traditional composite fabrication techniques can be easily manufactured with minimal expense, material waste, and machine setup time using 3D printing. With the necessity of building lightweight materials with high mechanical strength, AM can meet this demand. Fiber-reinforced thermoplastics have emerged as emerging materials in additive

*Corresponding Author. Email address: imuna@imp.gda.pl
https://doi.org/10.58139/wefn-t649

manufacturing due to their strength and stiffness without the need for multiple processes and special tools. For the matrix material, the advantage of employing thermoplastics such as polylactic acid (PLA), acrylonitrile butadiene styrene (ABS), polyether ether ketone (PEEK), etc in producing CFRP composites is their melt processability which can improve the manufacturing speed, lower the cost, and eliminate the prolonged cure cycles or complex curing chemistry. Another superiority of thermoplastics is that they can be manufactured using widely developed and readily available polymer AM methods.

During their life-time, understanding the effects of long-term thermal ageing is critical for better live performances of CFRP composites in order to avoid unexpected failure. A thorough understanding of the behavior of printing parts under constant thermal exposure can help predict their performance and serve to propose solutions for future improvements emerging in the industrial sectors. Many researchers have studied prolonged thermal effects on the mechanical properties of polymeric composites by applying thermal treatment at above zero degrees Celsius with most of the subjected parts manufactured using the traditional method [1–7]. Generally, the materials will undergo a lower strength at the macroscale due to induced micro-cracking of the matrix caused by thermal stress and chain-scission at the microscale. However, there is very little published data on the thermal treatment of 3D-printed polymer-based composites at subzero temperatures [8, 9]. So far, the researchers [10–14] have focused on sample parts printed with the FDM technique which were subjected to prolonged thermal exposure at above-zero temperatures. The aim of this paper is to characterize the morphological and thermal properties of 3D-printed composite parts after prolonged thermal treatment at various magnitudes. SEM micrographs reveal the porosity, defects, and damage within these structures which will indicate future directions for process optimization needed to obtain additively manufactured composite parts with desired properties.

2 Thermal analysis using DSC

2.1 DSC overview

The DSC method is a form of calorimetry, where the difference in heat flow between a test sample and a reference sample is measured during constant heating or cooling of the samples. Differential scanning calorimetry is a thermo-analytical technique that determines how much heat is required to raise a material's temperature. Differential scanning calorimetry (DSC) measures the energy absorbed (endotherm) or released (exotherm) as a function of time or temperature. It is used to characterize melting, crystallization, resin curing, loss of solvents, and other processes involving an energy change. Differential scanning calorimetry may also be applied to determine how much heat is required to raise a material's temperature processes (a change in heat capacity). Moreover, DSC rheology measurements are also suitable for detecting the effects of thermal degradation by observing the melting and crystallization process. Thermal degradation can also be observed through the complex viscosity which is very sensitive to chain modifications such as scission, branching, and cross-linking [15].

A DSC measuring cell consists of a furnace and an integrated sensor with designated positions for the sample and reference pans. The sample is placed in an aluminium pan, and the sample pan and an empty reference pan are placed on small platforms within the DSC chamber. Thermocouple sensors lie below the pans and they are connected to thermocouples. This allows for recording both the temperature difference between the sample and reference side (DSC signal) and the absolute temperature of the sample or reference side. The functional principle of an interior chamber of DSC is shown in Fig.1.

DSC measurements can be made in two ways: by measuring the electrical energy provided to heaters below the pans necessary to maintain the two pans at the same temperature (power compensation), or by measuring the heat flow (differential temperature) as a function of sample temperature (heat flux). The DSC ultimately outputs the differential heat flow (heat/time) between your material and the empty reference pan. Heat capacity may be determined by taking the ratio of heat flow to the heating rate. Therefore, $C_p = \frac{q}{\Delta T}$ where C_p is the material's heat capacity, q is the heat flow through the material over a given time, and ΔT is the change in temperature over that same time.

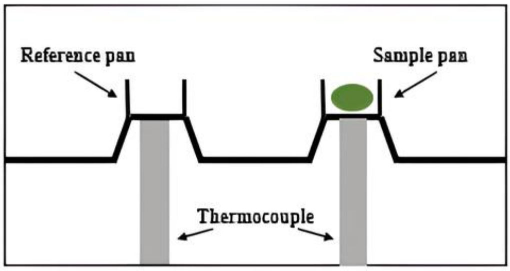

Figure 1: Schematic diagram of DSC interior chamber

Due to the heat capacity (C_p) of the sample, the reference side (usually an empty pan) generally heats faster than the sample side during the heating of the DSC measuring cell; for instance, the reference temperature (Tr, green) increases a bit faster than the sample temperature (Ts, green). The two curves exhibit parallel behavior during heating at a constant heating rate until a sample reaction occurs. In the case shown here, the sample starts to melt at t_1. The temperature of the sample does not change during melting; the temperature of the reference side, however, remains unaffected and continues exhibiting a linear increase. When melting is completed, the sample temperature also begins to increase again and, beginning with the point in time t_2, again exhibits a linear increase.

The differential signal (ΔT) of the two temperature curves is presented in the lower part of the image. In the middle section of the curve, the calculation of the differences generates a peak (blue) representing the endothermic melting process. Depending on whether the reference temperature was subtracted from the sample temperature or vice versa during this calculation, the generated peak may point upward or downward in the graphs. The peak area is correlated with the heat content of the transition (enthalpy in J/g). A typical DSC thermogram is shown in schematic Fig. 2 below.

2.2 DSC experimental procedure

Differential scanning calorimetry (DSC) was used to determine the glass transition temperature (Tg) of the polymeric composite samples in accordance with ASTM E1356. The melting temperature and crystallization temperature will also be analyzed according to ASTM E794. The purpose of the test was to determine whether there was any change in crosslinking of the PLA polymer, which could signify degradation as a result of the conditioning process. A DSC equipment (TA Instruments Q2000) was used to perform thermal analysis of the composite samples under controlled and isothermal conditions. The sample for each thermally treated group was chopped into small pieces to fit inside the pan due to the stiffness of the fiber-reinforced raw filament. There were 5 groups

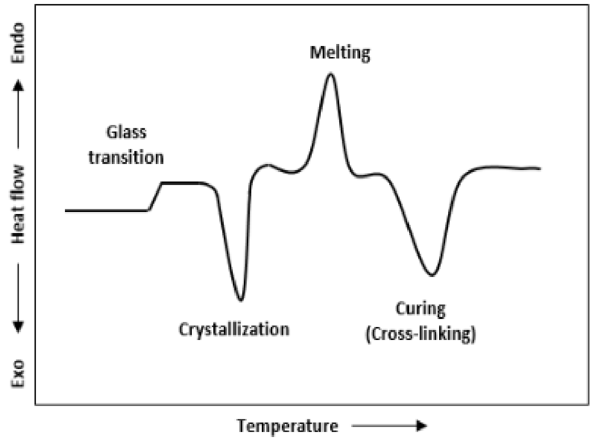

Figure 2: A schematic of a DSC thermogram

of printed CFRP samples for various thermal treatments as summarized in Tab. 1. The prepared samples then were measured with a precision scale. About 10 mg of sample from each treatment group was placed in an alumina hermetic pan and inserted into the DSC cell. A nitrogen atmosphere was supplied to the test chamber at a flow rate of 50 mL/min for the cooling process while an electrically heated furnace is used for heating. The temperature was ramped from 20°C to 200°C and then cooled back to 20°C at a heating and cooling rate of 10°C/min. The measurement for each sample consisted of two times of the heating process and one time of the cooling process. The following program was used: hold equilibrium at 24°C, ramp at 10°C/min to 200°C, hold isotherm for 2 min, ramp at 10°C/min to 40°C, hold isotherm for 2 min, and ramp back at 10°C/min to 200°C. The DSC equipment and DSC cell can be seen in Fig.3.

Table 1: Sample groups

Group name	Value
Intact	untreated samples
HS-A	hot stable at 65°C for 6 hours
HS-B	hot stable at 145°C for 6 hours
CS-A	cold stable at 0°C for 6 hours
CS-B	cold stable at -20°C, for 6 hours

Semicrystalline polymers are made up of two distinct phases: amorphous and crystalline. As a polymer becomes more crystalline, the fraction of the amorphous component decreases, and thus the change in the sample's C_p at Tg decreases. If the polymer becomes highly crystalline, the DSC instrument may eventually lose its sensitivity to detect Tg. In general, as the crystalline content of the polymer increases, so will the Tg temperature. The glass transition temperature is commonly abbreviated as Tg. Tg is the main characteristic transformation temperature of the amorphous phase and is produced by all

Figure 3: DSC equipment and DSC cell

amorphous (non-crystalline or semi-crystalline) materials during heating. When a hard, solid, amorphous material or component changes to a soft, rubbery, liquid phase, the glass transition phenomenon occurs. Tg is a valuable material characterization parameter that can provide very useful information about a product's end-use performance. The 'classic' Tg is observed as a stepwise endothermic change in the DSC heat flow or heat capacity.

2.3 DSC result analysis

Analysis of DSC curves for the initial heating, cooling, and second heating cycles of intact (untreated) and thermally treated CFRP specimens at stable and cyclic temperature modes are shown in Fig. 4. The important thermal phases such as glass transition (Tg), cold crystallization (Tcc), and melting point (Tm) temperature are studied to determine the polymer crystallinity. Glass transition temperature is indicated by a shift of the baseline from the initial DSC curves and reported glass transition temperature was based on the observed midpoint temperature. An exothermic peak indicates a cold crystallization where an exothermic reaction (heat release) has occurred, while an endothermic peak (heat adsorption) refers to the melting temperature in which an endothermic reaction takes place.

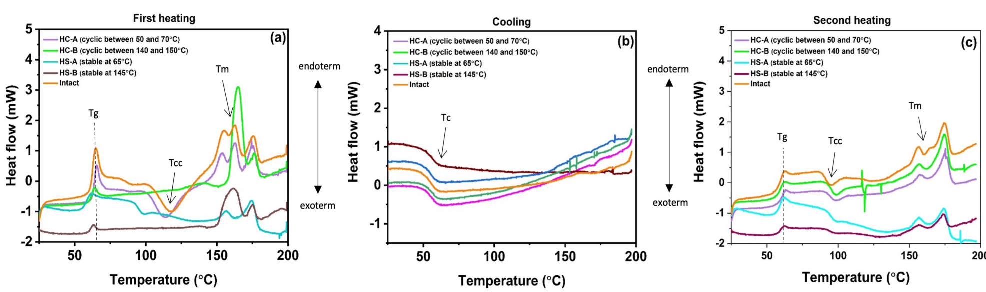

Figure 4: DSC graphs of 3D printed specimens: (a) First heating on thermally stable treatment groups; (b) Cooling on thermally stable treatment groups; (c) Second heating on thermally stable treatment groups

In the first heating process, the Tg of the untreated (intact) CFRP group falls at 65°C (midpoint) and is very much close to composites treated at a stable temperature at 0°C (CS-A). The specimens exposed to a stable subzero temperature at -20°C (CS-B) have slightly higher Tg compared to intact samples. The cold crystallization (Tcc) point of the intact group is observed to be the highest among treated groups indicated by an exothermal effect at a peak temperature of 117°C. Cold crystallization refers to the freezing of polymer chains in their amorphous state as a result of rapidly cooling a crystalline plastic from its liquid state. Crystallization is characterized by crystal nucleation and nucleus growth [16]. The cold crystallization process is distinguished by two characteristics: the promotion of nucleation as the supercooled glassy state gradually gains mobility with increasing temperature, and the presence of a maximum temperature for nucleation above which the cold crystallization process is diffusion limited [17]. The samples subjected to 65°C (HS-A group) have Tcc values of 98°C which is lower than the intact group. However, cold crystallization did not occur for the thermal group treated at 145°C (HS-B group) because the crystals do not have enough time to form. When reheating a material in this state, the formation of crystals causes an endothermic peak between the glass transition and the melting point.

In the first heating run, the double peak of melting temperatures was observed in all sample groups. This is due to the super-positioning of melting and recrystallization processes causing this behaviour. When the majority of the crystallization occurs during the cool-down process, the remaining amorphous regions lack place and chain mobility, resulting in imperfect crystals. These imperfect crystals begin to melt, but almost simultaneously, recrystallization occurs, resulting in the formation of a new crystal structure, which begins to melt almost immediately, forming the second peak [10]. During phase transitions, CFRP samples were observed to exhibit two distinct peaks (and onset points) which may indicate more than one form or crystal structure. Polylactic acid (PLA) is a polymer type used in the manufacturing process of CFRP composites and this thermoplastic has slow crystallization kinetics. In the case of PLA, three different crystallization processes can be identified with adequate experimental conditions: the classical cold crystallization and two processes associated with the non-reversing exotherms [18]. The DSC graphs obtained in this experiment exhibit unexpected and extraneous results such as non-reversing heat-flow curves with two exothermic processes and a larger endotherm in the middle. The multi-exothermic processes result from the occurrence of multiple crystalline states of PLA (α and β). The first peak at lower temperatures relates to the melting of the α crystalline state and its recrystallization into the α form, while the second peak at higher temperatures corresponds to the melting state β. The α - β phase transition is the transition from β to form following melting and recrystallization.

In the second heating process, the DSC curve produced lower values than the first run. The reason for this phenomenon is that the relaxation or molecular rearrangement already occurred in the first heating run, therefore the cooling process imparts/equilibrates the previously known history at a known rate from the first heating before heating again. As a result, any changes detected in the second heating curve between identical materials are due to actual internal differences in the materials (e.g., molecular weight) rather than previous thermal history effects. The cooling cycle gives the melt crystallization peak in each sample. The values of enthalpies obtained from the melting peak during the heating cycle and the melt crystallization peak during the cooling cycle are almost equal in each sample. This peak indicates the crystalline nature of the polymer. However, there are some cases when the reinforcement materials would constrain the PLA chains so much that the heat capacity jump becomes undetectable in DSC. Spatial confinement, nucleation on sample boundaries, temperature gradient, and melt flow are all important factors in polymer crystallization. Similarly, the presence of foreign substances in the pure PLA matrix influences PLA crystallization by assisting or hindering chain mobility.

3 Morphological analysis using scanning electron microscope (SEM)

Scanning electron microscopy (SEM) observation was carried out to evaluate the microstructure of specimens due to thermal treatment and the degradation of the polymer matrix, fibers, and interface was qualitatively evaluated using this observation. SEM device FE-SEM SU5000, Hitachi Co., Tokyo, Japan was utilized to investigate the micro-structural damage that resulted from tensile testing on various specimen groups. The largest specimen that the SEM could detect had dimensions of 200 mm in diameter and 80 mm in height.

The SEM images after thermal treatment are shown in Fig. 5. According to the SEM micrographs, the effect of prolonged thermal treatment on the 3D-printed CFRP specimens caused different microstructural fracture damages after tensile testing in both the polymers and carbon fibers when compared to the untreated (intact) specimens. The polymer structure of the intact sample structure was morphologically unseparated, and there was no breakage. The PLA polymers treated with prolonged temperature at 65°C exhibit smaller cracks compared to the sample group treated at 145°C. In the cold thermal treatment case, the prolonged temperature at -20°C (CS-B) has created some noticeable gaps in the fibers, and matrix crack was also presented with some fiber pull-out. For the treatment at 0°C (CS-A) fibers seemed to remain in their initial arrangement and the gaps between fibers were not observed. However, the PLA matrix is slightly distorted compared to the untreated (intact) group.

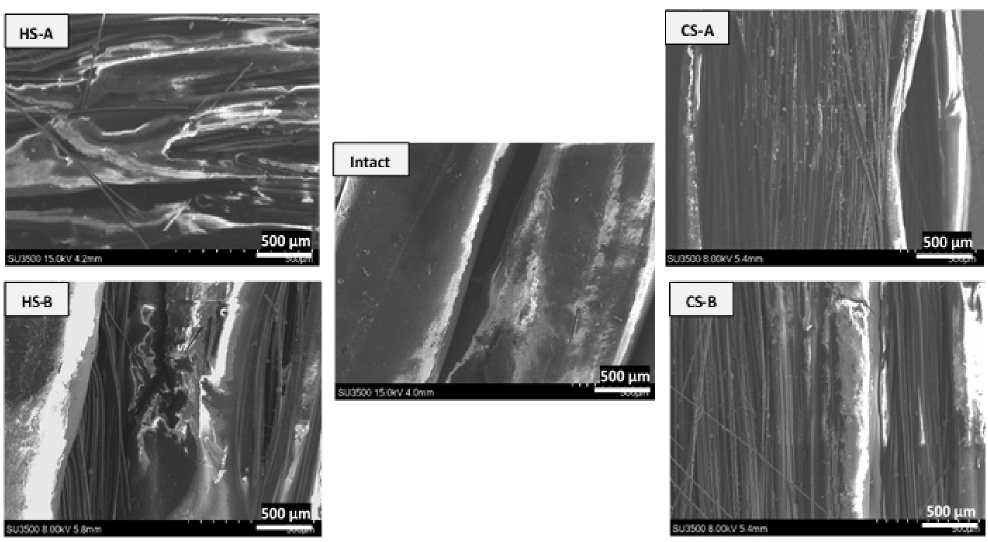

Figure 5: SEM photos of the untreated and treated specimen groups following destructive tensile testing.

4 Conclusion

In this paper, thermal and morphological characterization of additively manufactured CFRP composites under prolonged thermal loadings at above- and sub-zero temperatures were presented and discussed. After the manufacturing process, the thermal treatments at various magnitudes and modes were then subjected to the printed samples. Based on the thermal analysis using DSC testing, glass transition temperature (Tg), cold crystallization temperature (Tcc), and melting temperature (Tm) were studied. Cold crystallization did not occur when the specimens were exposed to the prolonged temperature at 145°C (HS-B group) because crystals are not given enough time to form. Since the cooling process equilibrates the previously known history at a known rate from the first heating before heating again, the first heating produced higher thermal values than the second heating run. As a result, any differences observed in the second heating curve between identical materials are due to actual internal material differences (e.g., molecular weight) rather than previous thermal history effects. During phase transitions, CFRP samples were found to have two distinct peaks (and onset points), indicating that they may have more than one form of crystal structure. The superpositioning of melting and recrystallization processes resulted in a double peak of melting temperatures. The visual inspection of the morphological surface shown in Fig. 5 revealed that the morphological surface changed slightly before and after the thermal treatment at subzero temperatures. The surface difference after the thermal treatment at above-zero temperatures is more noticeable.

The DSC curve confirmed a dried polymer matrix in the case of a CFRP sample exposed to continuous heating at 145°C by a smaller area of melting peak. The fracture interface of the 3D CFRP specimens, as well as changes in the matrix microstructure from each group, were examined using the SEM microscope. To investigate such outcomes, one specimen from each group that best reflected the failure mode was chosen. According to the findings, the higher the temperature exposure for above-zero degrees, the worse the damage in the polymer parts. The fibers had dried out during the heating process, making them more brittle than the groups that had been handled at lower temperatures. In the cold thermal treatment, a continuous temperature loading of -20°C (CS-B) caused some obvious gaps in the fibers, and a matrix break with some fiber pull-out was also seen. Fibers appeared to maintain their initial configuration during the 0°C (CS-A) treatment, and gaps between fibers were not seen.

5 Acknowledgement

The research was supported by the project entitled: Thermal degradation processes of additively manufactured structures (2019/35/O/ST8/00757) granted by the National Science Centre, Poland.

Received in June 2023.

References

[1] A. Ghasemi and M. Moradi, "Low thermal cycling effects on mechanical properties of laminated composite materials," *Mechanics of Materials*, vol. 96, pp. 126–137, 2016.

[2] M. Lafarie-Frenot and N. Ho, "Influence of free edge intralaminar stresses on damage process in cfrp laminates under thermal cycling conditions," *Composites Science and Technology*, vol. 66, no. 10, pp. 1354–1365, 2006.

[3] Z. Razak, A. B. Sulong, N. Muhamad, C. H. C. Haron, M. K. F. M. Radzi, N. F. Ismail, D. Tholibon, and I. Tharazi, "Effects of thermal cycling on physical and tensile properties of injection moulded kenaf/carbon nanotubes/polypropylene hybrid composites," *Composites Part B: Engineering*, vol. 168, pp. 159–165, 2019.

[4] C. Ma, D. Sánchez-Rodríguez, and T. Kamo, "Influence of thermal treatment on the properties of carbon fiber reinforced plastics under various conditions," *Polymer Degradation and Stability*, vol. 178, p. 109199, 2020.

[5] N. Hancox, "Thermal effects on polymer matrix composites: Part 1. thermal cycling," *Materials & Design*, vol. 19, no. 3, pp. 85–91, 1998.

[6] K. Shivakumar and A. Bhargava, "Failure mechanics of a composite laminate embedded with a fiber optic sensor," *Journal of composite materials*, vol. 39, no. 9, pp. 777–798, 2005.

[7] C. Lüders, D. Krause, and J. Kreikemeier, "Fatigue damage model for fibre-reinforced polymers at different temperatures considering stress ratio effects," *Journal of Composite Materials*, vol. 52, no. 29, pp. 4023–4050, 2018.

[8] O. Mysiukiewicz, M. Barczewski, and A. Kloziński, "The influence of sub-zero conditions on the mechanical properties of polylactide-based composites," *Materials*, vol. 13, no. 24, p. 5789, 2020.

[9] S. Kuciel, K. Mazur, and M. Hebda, "The influence of wood and basalt fibres on mechanical, thermal and hydrothermal properties of pla composites," *Journal of Polymers and the Environment*, vol. 28, pp. 1204–1215, 2020.

[10] M. Handwerker, J. Wellnitz, H. Marzbani, and U. Tetzlaff, "Annealing of chopped and continuous fibre reinforced polyamide 6 produced by fused filament fabrication," *Composites Part B: Engineering*, vol. 223, p. 109119, 2021.

[11] M. Zhang, B. Sun, and B. Gu, "Accelerated thermal ageing of epoxy resin and 3-D carbon fiber/epoxy braided composites," *Composites Part A: Applied Science and Manufacturing*, vol. 85, pp. 163–171, 2016.

[12] C. Pascual-González, P. San Martín, I. Lizarralde, A. Fernández, A. León, C. Lopes, and J. Fernández-Blázquez, "Post-processing effects on microstructure, interlaminar and thermal properties of 3D printed continuous carbon fibre composites," *Composites Part B: Engineering*, vol. 210, p. 108652, 2021.

[13] K. Wang, H. Long, Y. Chen, M. Baniassadi, Y. Rao, and Y. Peng, "Heat-treatment effects on dimensional stability and mechanical properties of 3D printed continuous carbon fiber-reinforced composites," *Composites Part A: Applied Science and Manufacturing*, vol. 147, p. 106460, 2021.

[14] Y. Ma, S. Jin, M. Ueda, T. Yokozeki, Y. Yang, F. Kobayashi, H. Kobayashi, T. Sugahara, and H. Hamada, "Higher performance carbon fiber reinforced thermoplastic composites from thermoplastic prepreg technique: Heat and moisture effect," *Composites Part B: Engineering*, vol. 154, pp. 90–98, 2018.

[15] M. Martín, F. Rodríguez-Lence, A. Güemes, A. Fernández-López, L. A. Pérez-Maqueda, and A. Perejón, "On the determination of thermal degradation effects and detection techniques for thermoplastic composites obtained by automatic lamination," *Composites Part A: Applied Science and Manufacturing*, vol. 111, pp. 23–32, 2018.

[16] E. Van Cappellen and A. Schmitz, "A simple spot-size versus pixel-size criterion for X-ray microanalysis of thin foils," *Ultramicroscopy*, vol. 41, no. 1-3, pp. 193–199, 1992.

[17] S. Vyazovkin, *Isoconversional kinetics of thermally stimulated processes.* Springer, 2015.

[18] C. A. Gracia-Fernández, S. Gómez-Barreiro, J. López-Beceiro, S. Naya, and R. Artiaga, "New approach to the double melting peak of poly (l-lactic acid) observed by DSC," *Journal of Materials Research*, vol. 27, no. 10, pp. 1379–1382, 2012.

Direct numerical simulations of particle-laden isotropic turbulence. Pseudo-spectral solver

Michał Rajek*

Institute of Fluid-Flow Machinery, Polish Academy of Sciences
14 Fiszera Street, 80-231 Gdansk, Poland

Abstract

In this work an in-house pseudo-spectral direct numerical simulations solver for particle-laden forced isotropic turbulence is developed. The code has been validated against the results of a decaying three-dimensional Taylor-Green vortex field at moderate Reynolds number. The solver can be relatively easily adapted for large-eddy simulations using the concept of spectral eddy-viscosity. The solver is coupled with the Lagrangian particle tracking of a dispersed phase essentially approximated by point-particles whose particle-to-fluid density ratio is $\mathcal{O}(10^3)$. High order Lagrange interpolation and combined implicit-explicit time-integration scheme are used to solve the particle equation of motion.

Keywords: pseudo-spectral; DNS; isotropic turbulence; inertial particles

1 Introduction

Turbulent dispersed multiphase flows are inherent part of many environmental and industrial processes. Among many others, this includes sand and dust storms, rain formation, sedimentation processes, cyclone separation, pharmaceutical sprays, fuel atomization and spray combustion. Obviously, an in-depth understanding of suspended particle dynamics in turbulent flows is of significant importance for further developments in the foregoing areas. Due to inevitable particle-turbulence and particle-particle interactions, possibly coupled with the heat-transfer, evaporation, or even chemical reactions, particle-laden turbulent flows are usually associated with multi-scale (or even multi-physics) complex phenomena yet to be fully understood, accurately predicted, and most importantly, controlled in order to obtain a desired change in the flow behavior. Due to a wide range of spatial and temporal scales, experimental investigations of dispersed turbulent multiphase flows often become problematic (or even unfeasible). On the other hand, it should be noted that both the continuous improvement of numerical methods and the rapid growth of computing capabilities provide a unique opportunity to study these complex flows. For a comprehensive review of recent advancements in the numerical simulation of particle-laden turbulent flows, the reader can refer to [1, 2].

Insofar as the physics underlying particle-laden flows is concerned, one should confine to the simplest examples of turbulent flows, usually associated with simple geometries. This includes for example the flow through a channel, past a sphere or a flat plate.

*Corresponding Author. Email address: mrajek@imp.gda.pl
https://doi.org/10.58139/c82v-cy47

Some assumptions can also be made regarding the dispersed phase. In the case of dilute suspensions of small particles, when compared to the smallest length scales of a turbulent flow, dispersed entities can usually be approximated by point-particles. The Lagrangian tracking of such individual mass-points can be effectively coupled with the Eulerian direct numerical simulations of the continuous carrier phase, essentially leading to the so-called point-particle direct numerical simulations.

In this work, the author restricts his attention to homogeneous isotropic turbulence which is considered as the most fundamental turbulent flow. In addition to that, isotropic turbulence can be realized (to some extent) experimentally [3]. The reader is also briefly acquainted with some key important elements of the pseudo-spectral solver developed for the purpose of studying suspended particle dynamics in homogeneous and isotropic turbulence.

2 The equations of fluid motion in Fourier space

In the case of an incompressible fluid, the continuity equation acquires the form of

$$\frac{\partial U_\alpha(\boldsymbol{x},t)}{\partial x_\alpha} = 0, \tag{1}$$

where $U_\alpha(\boldsymbol{x},t)$ is the fluid velocity at position $\boldsymbol{x}$ and time t. The conservation of momentum is governed by the Navier-Stokes equation in the form of

$$\frac{\partial U_\alpha}{\partial t} + U_\beta \frac{\partial U_\alpha}{\partial x_\beta} = -\frac{1}{\rho}\frac{\partial P}{\partial x_\alpha} + \nu \nabla^2 U_\alpha + F_\alpha, \tag{2}$$

where P is the pressure field, F is a body force, and ν is the kinematic viscosity of the fluid. For the sake of simplicity, the explicit dependence on both the position and time is dropped. According to the Reynolds decomposition [4], an arbitrary velocity field can be decomposed into the ensemble mean and a fluctuation about that mean leading to

$$U_\alpha = \langle U_\alpha \rangle + u_\alpha. \tag{3}$$

The flow can only be isotropic in the absence of preferential directions. This essentially implies the mean velocity is either zero or constant. In this work, the author confines his attention to turbulent flows for which

$$\langle U_\alpha \rangle = 0. \tag{4}$$

In fact, the above condition is often referred to as the zero-mean-flow condition. With the substitution of Eq. (3), and the use of Eq. (4), the equation governing the fluid motion, Eq. (2), can be rewritten to obtain

$$\frac{\partial u_\alpha}{\partial t} + u_\beta \frac{\partial u_\alpha}{\partial x_\beta} = -\frac{1}{\rho}\frac{\partial p}{\partial x_\alpha} + \nu \nabla^2 u_\alpha + f_\alpha, \tag{5}$$

which essentially describes the evolution of velocity fluctuations. In addition to Eq. (4), the velocity field (or the computational box, strictly speaking) must also be infinite in extent. In practice, the fluid is confined to a cubic box of side L_B, with periodic boundary conditions additionally imposed on its sides [5]. In this case, the velocity field can be expanded in a Fourier series according to

$$\begin{aligned} u_\alpha(\boldsymbol{x},t) &= \left(\frac{2\pi}{L_B}\right)^3 \sum_{\boldsymbol{k}} \hat{u}_\alpha(\boldsymbol{k},t) e^{i\boldsymbol{k}\cdot\boldsymbol{x}} \\ &= \left(\frac{2\pi}{L_B}\right)^3 \sum_{\boldsymbol{k}} \hat{u}_\alpha e^{i\boldsymbol{k}\cdot\boldsymbol{x}}, \end{aligned} \tag{6}$$

where $(\hat{\ })$ is used to distinguish the Fourier-transformed variables from their physical space counterparts; $\boldsymbol{k} = k_0\boldsymbol{n} = k_0(n_1\boldsymbol{e_1} + n_2\boldsymbol{e_2} + n_3\boldsymbol{e_3})$ is the wavevector with $k_0 = 2\pi L_B^{-1}$ being the lowest non-zero wavenumber; n_i are integers. In the case of $L_B \to \infty$, the Fourier transform, Eq. (6), takes the following integral form

$$u_\alpha = \int \mathrm{d}^3\boldsymbol{k}\ \hat{u}_\alpha e^{i\boldsymbol{k}\cdot\boldsymbol{x}}, \tag{7}$$

and

$$\hat{u}_\alpha = (2\pi)^{-3} \int \mathrm{d}^3\boldsymbol{x}\ u_\alpha e^{-i\boldsymbol{k}\cdot\boldsymbol{x}}. \tag{8}$$

In should noted that in the Fourier space the differential operator $\partial/\partial_{x_\alpha}$ is reduced to a simple complex multiplier ik_α. Taking advantage of this property, the continuity equation in the Fourier space becomes

$$ik_\alpha \hat{u}_\alpha = 0, \tag{9}$$

whereas with some minor rearrangement, the Navier-Stokes equation, Eq. (5), takes the form of

$$\frac{\partial \hat{u}_\alpha}{\partial t} + ik_\beta \mathcal{F}\left(u_\alpha u_\beta\right) = -ik_\alpha \frac{\hat{p}}{\rho} - \nu k^2 \hat{u}_\alpha + \hat{f}_\alpha, \tag{10}$$

where $\mathcal{F}$ denotes the Fourier transform, and $k^2 = k_\alpha k_\alpha = |\boldsymbol{k}|^2$. The pressure term on the right-hand side can be eliminated with the use of Eq. (9), eventually leading to

$$\left(\frac{\partial}{\partial t} + \nu k^2\right) \hat{u}_\alpha = -ik_\gamma P_{\alpha\beta}(\boldsymbol{k}) \mathcal{F}\left(u_\beta u_\gamma\right), \tag{11}$$

where $P_{\alpha\beta}(\boldsymbol{k}) = \delta_{\alpha\beta} - k_\alpha k_\beta / k^2$ is the projection tensor. Using the convolution theorem, the non-linear term can be evaluated by summing the Fourier coefficients leading to

$$\mathcal{F}(u_\beta u_\gamma) = \left(\frac{2\pi}{L_B}\right)^3 \sum_{\boldsymbol{p}+\boldsymbol{q}=\boldsymbol{k}} \hat{u}_\beta(\boldsymbol{p}) \hat{u}_\gamma(\boldsymbol{q}). \tag{12}$$

However, this requires $\mathcal{O}(N^2)$ operations where N is the number of nodes in each spatial direction. Obviously, the computational cost associated with the evaluation of Eq. (12) can become prohibitively large.

3 Pseudo-spectral approximation

Consider the velocity field $u_\alpha(\boldsymbol{x})$ defined on points of the discrete $N \times N \times N$ grid such that $x_\alpha = nL_B/N$ for $n = 0, 1, ..., N-1$, and whose Fourier coefficients $\hat{u}_\alpha(\boldsymbol{k})$ are defined for any $\boldsymbol{k}$ essentially satisfying $-N/2+1 \le k_\alpha \le N/2$. The velocity field is confined to a cubic box of side $L_B = 2\pi$, where periodic boundary conditions are imposed so that

$$u_\alpha(x_1 + 2\pi n_1, x_2 + 2\pi n_2, x_3 + 2\pi n_3) = u_\alpha(x_1, x_2, x_3, t), \tag{13}$$

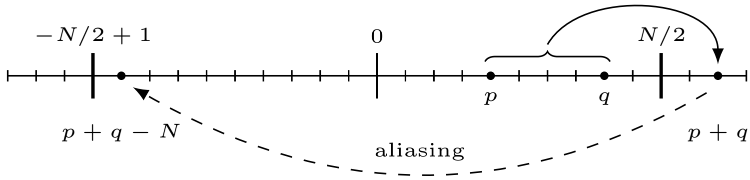

Figure 1: Aliasing errors arising from the application of the discrete Fourier transform.

where n_1, n_2, n_3 are integers. In this case, the velocity field (and the pressure field, obviously) can be expanded in the Fourier series according to Eq. (6). For completeness, the maximum resolved wavenumber in each spatial direction is $k_{\max} = k_0 N/2 = N/2$. Taking advantage of the convolution theorem, Eq. (12), Orszag [6] put forward the so-called pseudo-spectral approximation in which the non-linear term is first evaluated in the physical space, and then transformed back to the Fourier space. Using the Cooley & Tukey algorithm [7], often referred to as the Fast Fourier Transform (FFT) algorithm, the non-linear term can be evaluated in $\mathcal{O}(N\log N)$ operations. However, this comes at a price. The use of the discrete Fourier transform introduces the so-called aliasing errors, see Fig. 1, which should be removed in order to obtain reliable and stable numerical simulations. These errors are most often removed using the so-called "2/3" rule. In this method, the discrete Fourier transform is evaluated using M rather N points, where $M \geq 3/2N$. To get a more detailed description of this approach, the reader can refer to [8]. Patterson & Orszag [9] indicated that if the Fourier coefficients are truncated according to $|\boldsymbol{k}| \leq \sqrt{2}N/3$, then the aliasing errors are significantly reduced. The very same authors reported that the remaining part of the aliasing errors can be effectively removed if the convolution sum, Eq. (12), is evaluated at two grids shifted by half a grid cell in each direction, and subsequently averaged. In this work, the author removes the aliasing errors using the combined approach proposed by Patterson & Orszag. This dealiasing scheme, although being less efficient than the "2/3" rule, allows to retain more Fourier modes and thus becomes a method of choice when memory is a concern.

Due to numerical stability [10], the Navier-Stokes equation, Eq. (5), is often expressed in the rotation form which can be transformed to the Fourier space according to

$$\left(\frac{\partial}{\partial t} + \nu k^2\right) \hat{u}_\alpha = P_{\alpha\beta}\mathcal{F}(\boldsymbol{u}\times\boldsymbol{\omega})_\beta + \hat{f}_\alpha, \tag{14}$$

where $\boldsymbol{\omega}$ is the vorticity field in the physical space, and $\hat{f}_\alpha$ is an artificial forcing used to sustain turbulence.

In this work, the author uses a deterministic forcing similar to that introduced in [11] and [12], i.e.,

$$\hat{f}_\alpha(\boldsymbol{k}) = \begin{cases} (\epsilon_f/2E_f)u_\alpha(\boldsymbol{k}) & 0 < k < k_f \\ 0 & \text{otherwise}, \end{cases} \tag{15}$$

where ϵ_f is the energy injection rate, E_f is the total kinetic energy contained in the forced wavenumber band, and k_f is the maximum forced wavenumber, usually not exceeding $2\sqrt{2}$. The forcing has to be adjusted so that both the smallest, dissipative scales, and the largest, energy containing scales are accurately resolved on a finite grid.

4 Time integration of the Navier-Stokes equations

Stable and accurate integration of the equations governing the fluid motion requires the spatial and temporal discretization errors to be kept at a relatively low level. According to the best of the author's knowledge, the viscous term in the Navier-Stokes equation is usually integrated implicitly using the integrating factor technique [13, 14], wheres the explicit second-order (also third- and fourth-order) Runge-Kutta [15, 16] or second-order Adams-Bashforth [17] methods are employed to advance the convective term in time. Some authors also combined the implicit Crank-Nicolson and second-order Adams-Bashforth methods for viscous and convective term, respectively [18].

Introducing a time step, such that $t_n = n\Delta t$, the velocity field can be advanced in time according to

$$\begin{aligned}\hat{u}_\alpha^{n+1} = \hat{u}_\alpha^n e^{-\nu k^2 \Delta t} + \frac{\Delta t}{24}\Big[&55\Pi^n e^{-\nu k^2 \Delta t} - 59\Pi^{n-1} e^{-2\nu k^2 \Delta t} + \\ &37\Pi^{n-2} e^{-3\nu k^2 \Delta t} - 9\Pi^{n-3} e^{-4\nu k^2 \Delta t}\Big],\end{aligned} \tag{16}$$

where

$$\Pi^n = P_{\alpha\beta}\hat{N}_\beta^n + \hat{f}_\alpha^n. \tag{17}$$

It should be noted that the forcing term, $\hat{f}_\alpha$, is in general designed to be solenoidal and statistically isotropic, and thus can be safely added to the non-linear term before the projection tensor is applied leading to

$$\Pi^n = P_{\alpha\beta}(\hat{N}_\beta^n + \hat{f}_\beta^n). \tag{18}$$

In fact, this minor modification corrects the round-off errors resulting from the repeated evaluation of the discrete Fourier transforms, thus allowing long-term time-integration of the Navier-Stokes equation. The foregoing scheme, essentially composed of the integrating factor technique and the fourth-order Adams-Bashforth methods, seems to constitute a reasonable trade-off between accuracy and the computational cost of the simulation.

5 Preliminary results

In this section some results are compared against the reference data reported in [19] for a three-dimensional, incompressible Taylor-Green vortex at $Re = 1600$. This vortex field essentially develops from a single-mode initial condition defined according to

$$\begin{aligned} u_1(\boldsymbol{x}, t=0) &= \sin(x_1)\cos(x_2)\cos(x_3) \\ u_2(\boldsymbol{x}, t=0) &= -\cos(x_1)\sin(x_2)\cos(x_3) \\ u_3(\boldsymbol{x}, t=0) &= 0, \end{aligned} \tag{19}$$

and was first considered by Taylor & Green [20] who studied the generation of small-scale turbulence. It is readily apparent from Figs. 2 and 3 that the results are in good agreement with the reference data. Some discrepancies are readily observed, however, these can presumably be attributed to the insufficient spatial resolution. In should emphasized that the results reported in this work were obtained on a 64^3 discrete grid, whereas the reference simulations were carried on a much denser one, i.e. 512^3. For completeness, the author would to like to stress that with increasing spatial resolution, the foregoing differences are significantly reduced (not shown).

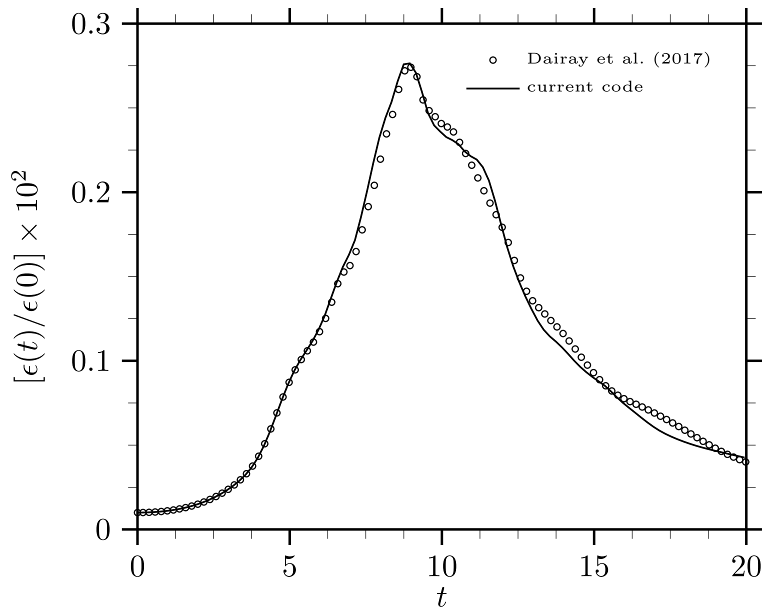

Figure 2: Time history of the normalized energy dissipation at $Re = 1600$. Reference data obtained from [19].

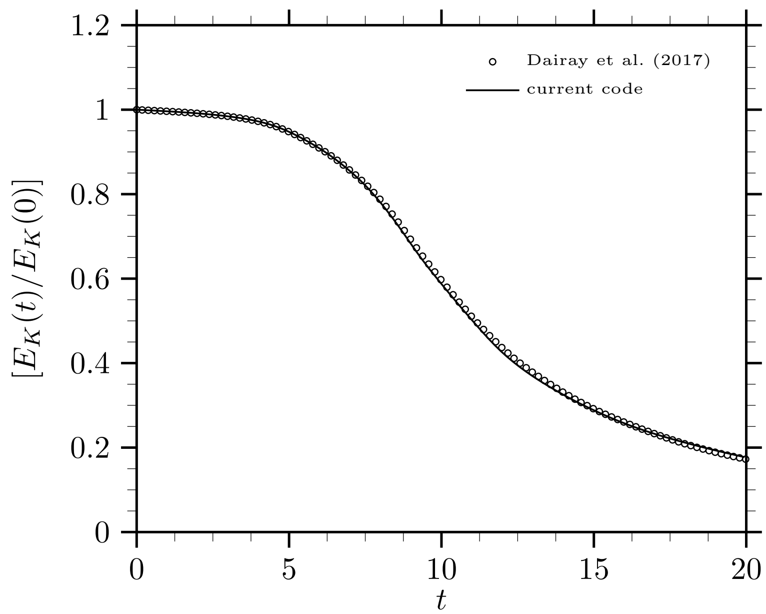

Figure 3: Time history of the normalized energy at $Re = 1600$. Reference data obtained from [19].

6 Lagrangian particle tracking

Consider a small rigid sphere of radius a whose mass is centered at $\boldsymbol{Y}(t)$, which is essentially moving with velocity $V_\alpha(t)$ in an undisturbed velocity field $u_\alpha(\boldsymbol{x},t)$. If the particle-fluid density ratio is large, say $> 10^3$, than the well-known Maxey & Riley [21] equation of particle motion takes the form of

$$\begin{aligned}\frac{\mathrm{d}V_\alpha}{\mathrm{d}t} &= -f_D\frac{V_\alpha - u_\alpha[\boldsymbol{Y}(t),t]}{\tau_p} + g_\alpha\\ \frac{\mathrm{d}Y_\alpha}{\mathrm{d}t} &= V_\alpha,\end{aligned} \tag{20}$$

where $\tau_p = 2\rho_p a^2/9\mu$ is the particle response time; μ is the dynamic viscosity of the fluid, ρ_p is the particle density; $u_\alpha[\boldsymbol{Y}(t),t]$ denotes the fluid velocity at the particle location, and $\boldsymbol{g}$ is the gravitational acceleration. The non-dimensional correction factor

$$f_D = 1 + 0.15Re_p^{0.687} \qquad Re_p < 1000 \tag{21}$$

was proposed by Schiller & Neumann [22] to account for the drag force beyond the Stokes flow regime. In the equation above Re_p is the so-called particle Reynolds number defined as

$$Re_p = \frac{\left|\boldsymbol{V} - \boldsymbol{u}\left[\boldsymbol{Y}(t),t\right]\right|d}{\nu}, \tag{22}$$

where d is the particle diameter.

7 Fluid velocity at the particle location

It is readily apparent from Eq. (20) that prior to solving the particle equation of motion, one has to determine the fluid velocity at the particle location. As already indicated, if the velocity field is expanded in the Fourier series, Eq. (6), then the fluid velocity at the instantaneous particle location can be determined by summing the Fourier coefficients. Obviously, the computational cost of this approach can quickly become prohibitively large. In the pseudo-spectral approximation, however, the velocity field is Fourier-transformed to the physical space at each time step, and thus can be relatively easily interpolated to the instantaneous particle locations. For a comprehensive review of various interpolation schemes, one can refer to [23].

Consider an example of a one-dimensional interpolation given in Fig. 4. In this case, the value of an arbitrary function $f(x_p)$ is approximated by

$$f(x_p) \approx \sum_{i=1}^{6} f(x_i)L_i(x_p), \tag{23}$$

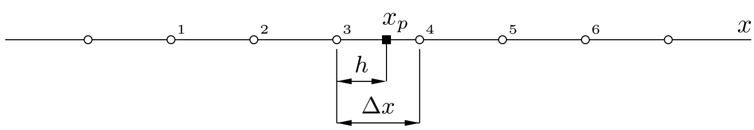

Figure 4: Six-point, one-dimensional Lagrange interpolation; x_p denotes the instantaneous particle location.

where $L_i(x_p)$ are the standard Lagrange basis functions determined at three grid points lying either side of x_p according to

$$L_i(x_p) = \prod_{k=1,k\neq i}^{6} \frac{x_p - x_k}{x_i - x_k}, \tag{24}$$

and thus

$$\begin{aligned} L_1(x_p) &= \frac{x_p - x_2}{x_1 - x_2}\frac{x_p - x_3}{x_1 - x_3}\frac{x_p - x_4}{x_1 - x_4}\frac{x_p - x_5}{x_1 - x_5}\frac{x_p - x_6}{x_1 - x_6} = \\ &= \frac{1}{120}\left(6p - 5p^2 - 5p^3 + 5p^4 - p^5\right), \end{aligned} \tag{25}$$

where $p = h/\Delta x$ with h being the distance between the particle and its closest left neighbor. The full set of basis functions for a one-dimensional Lagrangian interpolation is therefore given by

$$\begin{aligned} L_1(x_p) &= \frac{1}{120}(6p - 5p^2 - 5p^3 + 5p^4 - p^5) \\ L_2(x_p) &= \frac{1}{24}(-12p + 16p^2 - p^3 - 4p^4 + p^5) \\ L_3(x_p) &= \frac{1}{12}(12 - 4p - 15p^2 + 5p^3 + 3p^4 - p^5) \\ L_4(x_p) &= \frac{1}{12}(12p + 8p^2 - 7p^3 - 2p^4 + p^5) \\ L_5(x_p) &= \frac{1}{24}(-6p - p^2 + 7p^3 + p^4 - p^5) \\ L_6(x_p) &= \frac{1}{120}(4p - 5p^3 + p^5) \end{aligned} \tag{26}$$

It can be readily noticed that for a set of N_p particles the foregoing sixth-order Lagrangian interpolation scheme requires $3\times 6^3 \times N_p$ operations to determine the local fluid velocity at the instantaneous particle location, and additionally $3 \times 6^2 \times N_p$ operations to determine the corresponding basis functions.

Using the sixth-order, three-dimensional Lagrangian interpolation scheme, the velocity field at the instantaneous particle location $\boldsymbol{Y}(t) = (x_p, y_p, z_p)$ can be approximated according to

$$u_\alpha(x_p, y_p, z_p) \approx \sum_{i=1}^{6}\sum_{j=1}^{6}\sum_{l=1}^{6} u_\alpha(x_i, y_j, z_l) L_i(x_p) L_j(y_p) L_l(z_p). \tag{27}$$

8 Time integration of the particle equation of motion

In this work, the particle velocity is advanced in time using both the fifth-order implicit Adams-Moulton and the fourth-order explicit Adams-Bashforth schemes essentially leading to

$$V_\alpha^{n+1} = V_\alpha^n - f_D^n\left(\frac{\Delta t'}{720}\Pi_\alpha^{AM} - \frac{\Delta t'}{24}\Pi_\alpha^{AB}\right) \tag{28}$$

where $\Delta t' = \Delta t/\tau_p$, and

$$\begin{aligned} \Pi_\alpha^{AM} &= 251V_\alpha^{n+1} + 646V_\alpha^{n-1} - 264V_\alpha^{n-2} + 106V_\alpha^{n-3} \\ &\quad - 19V_\alpha^{n-4}. \end{aligned} \tag{29}$$

The remaining term on the right-hand side can be determined using

$$\Pi_\alpha^{AB} = 55u_\alpha^n - 59u_\alpha^{n-1} + 37u_\alpha^{n-2} - 9u_\alpha^{n-3}. \tag{30}$$

With the use of Eq. (28), particle trajectories can be advanced in time according to

$$Y_\alpha^{n+1} = Y_\alpha^n + \frac{\Delta t'}{720}\Pi_\alpha^{AM}. \tag{31}$$

9 Conclusions and outlook

In this work, the current stage of development of the pseudo-spectral direct numerical simulations solver intended for studying suspended particle dynamics in homogeneous isotropic turbulence was presented. Preliminary validation indicates that the DNS solver can be considered accurate and reliable. Next steps include the validation of the particulate-phase solver, and the extension of the momentum conservation equation with specific source terms in order to account for the particle-turbulence interaction. In addition to that, the LES solver is to be implemented. However, the last step is rather straightforward and essentially boils down to extending the Navier-Stokes equation, Eq. (14), with the spectral eddy-viscosity ν_e according to

$$\left(\frac{\partial}{\partial t} + \left[\nu + \nu_e(k|k_c)\right]k^2\right)\hat{u}_\alpha = P_{\alpha\beta}\mathcal{F}(\boldsymbol{u}\times\boldsymbol{\omega})_\beta + \hat{f}_\alpha, \tag{32}$$

where, following Chollet & Lesieur [24],

$$\nu_e(k/k_c) = C_K^{-3/2}\left(0.441 + 15.2e^{-3.03k_c/k}\right)\sqrt{\frac{E(k_c)}{k_c}}. \tag{33}$$

In the equation above, C_K is set to 1.4, k_c is a prescribed cutoff wavenumber, and $E(k_c)$ is the kinetic energy density at the cutoff.

Acknowledgments

The work was supported by the National Science Centre (NCN, Poland), research project 2018/30/Q/ST8/00341, and the statutory activities of IMP PAN Gdańsk.

Received in September 2023

References

[1] J. Kuerten, "Point-particle DNS and LES of particle-laden turbulent flow – a state-of-the-art review," *Flow, Turbulence and Combustion*, vol. **97**, pp. 689–713, 2016.

[2] S. Elghobashi, "Direct numerical simulation of turbulent flows laden with droplets or bubbles," *Annual Review of Fluid Mechanics*, vol. **51**, pp. 217–244, 2019.

[3] W. McComb, *The Physics of Fluid Turbulence.* Oxford University Press, Oxford.

[4] O. Reynolds, "On the dynamical theory of incompressible viscous fluids and the determination of the criterion," *Philosophical Transactions of the Royal Society A*, vol. **186**, pp. 123–164, 1894.

[5] D. Leslie, *Developments in the Theory of Turbulence.* Clarendon Press, Oxford, 1990.

[6] S. Orszag, "Numerical methods for the simulation of turbulence," *Physics of Fluids*, vol. **12**, pp. II–250, 1969.

[7] J. Cooley and J. Tukey, "An algorithm for the machine calculation of complex fourier series," *Mathematics of Computation*, vol. **19**, pp. 297–301, 1965.

[8] C. Canuto, M. Hussaini, A. Quarteroni, and T. A. Zang, *Spectral Methods in Fluid Dynamics.* Springer-Verlag, New York, 1987.

[9] G. Patterson Jr and S. Orszag, "Spectral calculations of isotropic turbulence: Efficient removal of aliasing interactions," *Physics of Fluids*, vol. **14**, pp. 2538–2541, 1971.

[10] S. Orszag, "Numerical simulation of incompressible flows within simple boundaries. I. Galerkin (spectral) representations," *Studies in Applied Mathematics*, vol. **50**, pp. 293–327, 1971.

[11] A. Witkowska, D. Juvé, and J. Brasseur, "Numerical study of noise from isotropic turbulence," *Journal of Computational Acoustics*, vol. **5**, pp. 317–336, 1997.

[12] L. Machiels, "Predictability of small-scale motion in isotropic fluid turbulence," *Physical Review Letters*, vol. **79**, p. 3411, 1997.

[13] A. Young, *Investigation of Renormalization Group Methods for the Numerical Simulation of Isotropic Turbulence.* Ph.D. dissertation, University of Edinburgh, 2002.

[14] S. Yoffe, *Investigation of the Transfer and Dissipation of Energy in Isotropic Turbulence.* Ph.D. dissertation, University of Edinburgh, 2012.

[15] V. Eswaran and S. Pope, "An examination of forcing in direct numerical simulations of turbulence," *Computers & Fluids*, vol. **16**, pp. 257–278, 1988.

[16] N. Sullivan, S. Mahalingam, and R. Kerr, "Deterministic forcing of homogeneous, isotropic turbulence," *Physics of Fluids*, vol. **6**, pp. 1612–1614, 1994.

[17] A. Vincent and M. Meneguzzi, "The spatial structure and statistical properties of homogeneous turbulence," *Journal of Fluid Mechanics*, vol. **225**, pp. 1–20, 1991.

[18] L.-P. Wang and M. Maxey, "Settling velocity and concentration distribution of heavy particles in homogeneous isotropic turbulence," *Journal of Fluid Mechanics*, vol. **256**, pp. 27–68, 1993.

[19] T. Dairay, E. Lamballais, S. Laizet, and J. Vassilicos, "Numerical dissipation vs. subgrid-scale modelling for large eddy simulation," *Journal of Computational Physics*, vol. **337**, pp. 252–274, 2017.

[20] G. Taylor and A. Green, "Mechanism of the production of small eddies from large ones," *Proceedings of the Royal Society of London. Series A-Mathematical and Physical Sciences*, vol. **158**, pp. 499–521, 1937.

[21] M. Maxey and J. Riley, “Equation of motion for a small rigid sphere in a nonuniform flow,” *Physics of Fluids*, vol. **26**, pp. 883–889, 1983.

[22] L. Schiller and A. Z. Naumann, “Über die grundlegenden berechungen bei der schwerkraftaufbereitun,” *Zeitschrift des Vereines Deutscher Ingenieure*, vol. **77**, pp. 318–320, 1933.

[23] S. Balachandar and M. Maxey, “Methods for evaluating fluid velocities in spectral simulations of turbulence,” *Journal of Computational Physics*, vol. **83**, pp. 96–125, 1989.

[24] J.-P. Chollet and M. Lesieur, “Parameterization of small scales of three-dimensional isotropic turbulence utilizing spectral closures,” *Journal of Atmospheric Sciences*, vol. **38**, pp. 2747–2757, 1981.

Deep learning-based approach for delamination identification using animation of Lamb waves propagation

Saeed Ullah*

Institute of Fluid-Flow Machinery, Polish Academy of Sciences
14 Fiszera Street, 80-231, Gdansk, Poland

Abstract

Composite materials are prone to various kinds of defects in their service life, among which delamination is a very hazardous type of damage. The traditional visual inspection techniques often fail to detect delamination in composite structures. Guided Lamb waves are increasingly being applied for the identification of delamination in these structures. Scanning laser Doppler vibrometry can measure the full wavefield of guided Lamb waves, such full wavefield contains rich information about defects. In this research work, a novel deep learning-based semantic segmentation technique is applied for delamination identification on full wavefield data. A big dataset of full wavefield images resulting from the interaction with delamination of random shape, size, and location was utilised and fed into the proposed deep learning model. The main motive of this research work is to investigate the applicability of deep learning-based approach for delamination identification in composite structures by using only the animations of guided Lamb waves. It is verified that the performance of the proposed deep learning model is good. Moreover, it enables better automation of identification of delamination, which can further produce damage maps without the intervention of the user. Furthermore, the developed deep learning model also indicates the capability of generalising well to the experimental data.

Keywords: Lamb waves; Delamination identification; Semantic segmentation; Deep learning; ConvLSTM

1 Introduction

These days, composite materials are extensively used for acquiring the desired performance in a broad range of industries, such as aerospace, wind turbines, automotive, marine, and many more. This extensive use of composite materials is due to their considerable advantages, such as lightweight, low cost, high strength, higher stiffness-to-mass ratio compared to metals, and effective corrosion resistance [1–3]. However, these materials are prone to different kinds of defects such as cracks, fiber breakage, debonding, and delamination [3, 4]. Among these defects, delamination is one of the most hazardous forms

*Corresponding Author. Email address: sullah@imp.gda.pl
https://doi.org/10.58139/qh7d-kh13

of defects in composite materials. Delamination diminishes the life of these structures and can lead to catastrophic failures if not detected at an early stage [4, 5]. Therefore, for the safe operation of these structures, it is essential to identify the delamination effectively.

The detection of delamination in composite materials is very challenging for conventional visual inspection techniques because it occurs between plies of composite laminate and is invisible from external surfaces [6, 7]. Accordingly, different types of nondestructive testing (NDT) and structural health monitoring (SHM) techniques have been proposed for delamination identification in composite structures. Among various damage identification techniques, ultrasonic guided waves are widely known as one of the most promising techniques for the quantitative identification of defects in composite structures. The widespread applications of these waves are due to their higher sensitivity to small defects, propagation with low attenuation, and potential to monitor large areas and the need of only a small number of sparsely distributed transducers [8–10].

However, utilising a smaller number of transducers is not appropriate for acquiring high-quality resolution damage maps and the assessment of damage size. On the other hand, the employment of a very dense array of transducers is also not feasible in most situations. To alleviate such problems, a scanning laser Doppler vibrometer (SLDV) is employed. SLDV is capable of measuring the propagation of guided waves in a highly dense grid of points over the surface of a large specimen. This collection of signals is known as full wavefield [11]. In recent years, full wavefield signals have been used for the detection and localisation of defects in composite structures [11–14]. Damage identification techniques employing full wavefield signals are capable of effectively estimating not only the location but also the size of damage [12, 13]. Full wavefields provide valuable information regarding the interaction of guided Lamb waves with potential defects. However, these full wavefields are very complex. Analysing such wavefields is very difficult for conventional physics or classical machine learning-based models.

Conversely, deep learning, which is originated from the artificial neural network (ANN), is capable of handling such complex and nonlinear data and has shown very promising results in different domains such as computer vision, object detection, speech recognition, remote sensing, medical sciences, and many more [15–17]. In recent years, deep learning has also shown significant improvements in image segmentation due to the advancement of deep convolutional neural networks (CNNs). Deep learning-based systems intend to derive hierarchical representations from the input data via constructing deep neural networks with multiple layers of non-linear transformations. In deep learning architectures, the output of one layer acts as the input to the next subsequent layer. The stacking composition of many layers enables the model to learn complex patterns from raw input data. Therefore, these systems do not need extensive human labour and knowledge for hand-crafted feature design [18].

Different researchers have applied basic ANN and deep learning architectures for damage identification in composite structures by employing thermography, vibration, and frequency-based approaches [19–22]. Furthermore, many researchers have also applied ANN and deep learning-based approaches for damage identification in composite structures by utilising guided Lamb waves [23–30].

In this work, the author applied a deep learning model on the full wavefield frames of propagating Lamb waves. This means that there is no need of any signal post-processing technique like for example RMS. Consequently, a many-to-one prediction scheme (many input frames to damage map) was used in the proposed deep learning model. In simple words, a sequence of full wavefield frames (animation) is fed into the proposed deep learning model. The proposed model is inspired by convolutional long short-term memory (ConvLSTM) architecture and tailored to the particular problem of delamination identification. Two classes (damaged and undamaged) were defined in the pixel-wise segmentation problem.

To the best of the author knowledge, it is the first implementation of deep neural networks utilising Lamb wave propagation animations for damage imaging with semantic segmentation. The proposed model showed excellent capabilities to identify the delamination in the numerically generated dataset. Moreover, the developed model can generalise well, therefore, the proposed model could be used for delamination identification in real-world scenarios. This is confirmed through the experiments on CFRP plates with single and multiple delaminations.

2 Image segmentation

It is not justified to process the entire image at the same time as there maybe regions in the image which do not contain any useful information. By dividing the image into segments, only the important segments can be used for processing the image. That, in a nutshell, is how image segmentation works. Image segmentation is a fundamental component in numerous visual recognition systems. In the last few years, image segmentation has widely been employed in autonomous driving [31, 32], medical applications [33], agriculture sciences [34], augmented reality [35] and many more. The purpose of image segmentation is to partition images or video frames into multiple objects or segments [36]. It can be expressed as a pixel-level classification problem with semantic labels, which is known as semantic segmentation, or partitioning the images into individual objects, which is called instance segmentation [36, 37]. Semantic segmentation functions on pixel-wise labeling with a set of object categories for an image. Therefore, it is generally a more difficult task than image classification, which only predicts a single label for the entire image [37]. Furthermore, semantic image segmentation not only depends on the semantics in the question but also on the problem that needs to be addressed [38].

3 The dataset

In this work, a synthetic dataset of propagating waves in carbon fibre reinforced composite plates was computed by using the parallel implementation of the time domain spectral element method [39]. Essentially, the dataset resembles the particle velocity measurements at the bottom surface of the plate acquired by the SLDV in the transverse direction as a response to the piezoelectric (PZT) excitation at the centre of the plate. The input signal was a five-cycle Hann window modulated sinusoidal tone burst. The carrier frequency was assumed to be 50 kHz. The total wave propagation time was set to 0.75 ms so that the guided wave could propagate to the plate edges and back to the actuator twice. The number of time integration steps was 150000, which was selected for the stability of the central difference scheme.

The material was a typical cross-ply CFRP laminate. The stacking sequence $[0/90]_4$ was used in the model. The properties of a single ply were as follows [GPa]: $C_{11} = 52.55$, $C_{12} = 6.51$, $C_{22} = 51.83, C_{44} = 2.93, C_{55} = 2.92, C_{66} = 3.81$. The assumed mass density was 1522.4 kg/m^3. These properties were selected so that they simulated numerically wave front patterns and wavelengths that are similar to the wavefields measured by SLDV on CFRP specimens used later on for testing the developed approach for delamination identification. The shortest wavelength of the propagating A0 Lamb wave mode was 21.2 mm for numerical simulations and 19.5 mm for experimental measurements.

475 cases were simulated, representing Lamb waves propagation and interaction with single delamination for each case. The following random factors were used in simulated delamination scenarios:

- delamination geometrical size $2b$ and $2a$, namely ellipse minor and major axis randomly selected from the interval $[10\,\mathrm{mm}, 40\,\mathrm{mm}]$,
- delamination angle α randomly selected from the interval $[0°, 180°]$,
- coordinates of the centre of delamination (x_c, y_c) randomly selected from the interval $[0\,\mathrm{mm}, 250\,\mathrm{mm} - \delta]$ and $[250\,\mathrm{mm} + \delta, 500\,\mathrm{mm}]$, where $\delta = 10\,\mathrm{mm}$).

These parameters are defined in Fig. 1 which illustrates exemplary possible locations, sizes, and shapes of random delaminations used for Lamb wave propagation modeling. It should be noted that the numerical cases include delaminations located at the edge and corners of the plate.

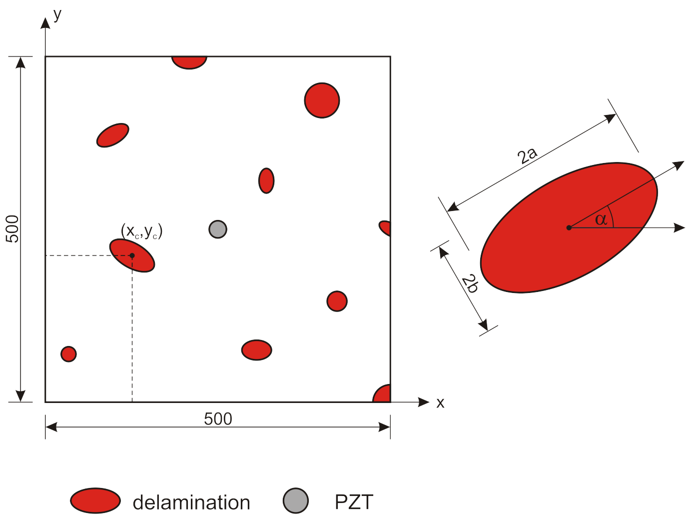

Figure 1: Exemplary locations, sizes and shapes of random delaminations used for Lamb wave propagation modeling.

The dataset contains frames of propagating waves (512 frames for each delamination scenario) and is available online [40]. The synthetic dataset is used for training the proposed neural network architecture with the aim of delamination identification directly from SLDV measurements without the need for a baseline wavefield.

Fig. 2 shows selected frames at different time-steps of the propagating Lamb waves before and after the interaction with the delamination. Frame f_1 represents the initial interactions with the delamination, which was calculated using the delamination location and the velocity of the $A0$ Lamb wave mode. While frame f_m represents the last frame in the training sequence window, accordingly, $m = 64$ for the proposed model, which will be discussed in the next section. The dataset contains 475 different cases, with 512 frames per case, producing a total number of $243,200$ frames with a frame size of (500×500) pixels representing the geometry of the specimen of size (500×500) mm^2.

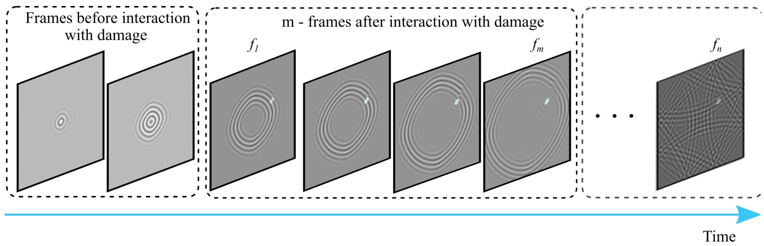

Figure 2: Sample frames of full wave propagation.

For training and evaluation of the proposed deep learning model, the dataset was divided into two sets: training and testing, with a ratio of 80% and 20% respectively. Moreover, 10% of the training set was preserved as a validation set to validate the model during the training process. Additionally, the dataset was normalised to a range of $(0, 1)$ to improve the convergence of the gradient descent algorithm. The author selected 64 consecutive frames in each delamination case as using all frames in each case has high computational and memory costs. Additionally, frames displaying the propagation of guided waves before interaction with the delamination has no features to be extracted. Hence, only a certain number of frames were selected from the initial occurrence of the interactions with the delamination (see Fig. 2 for details).

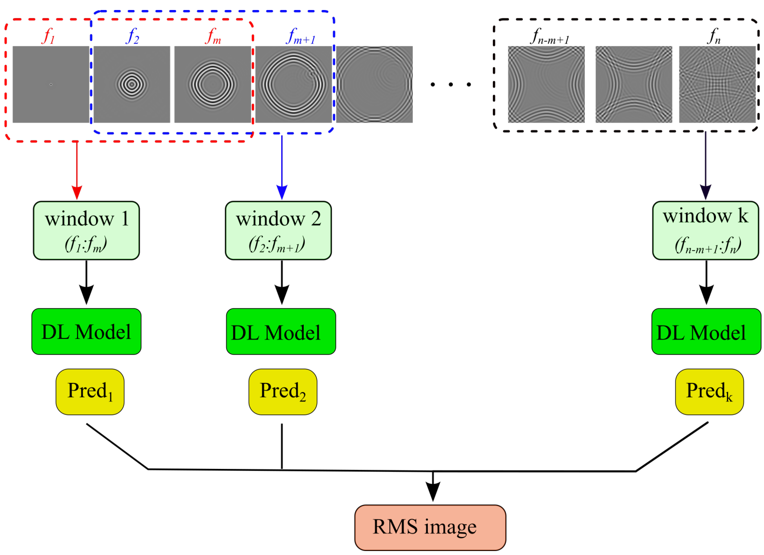

Figure 3: The procedure of calculating the RMS prediction image.

Fig. 3 illustrates the complete procedure of obtaining the intermediate predictions for the testing cases and finally calculating the RMS image. Where f_1 refers to the starting frame and f_n is the last frame, $(n = 512)$ in the dataset. Further, m refers to the number of frames in the window, which is 64 frames for the proposed model, and k represents the total number of windows. Accordingly, the author slide the window over all input frames. The shift of the window is one frame at a time.

4 Introduction to RNN, LSTM and ConvLSTM

Feed-forward neural networks such as traditional ANNs and CNNs cannot learn temporal features from the data and hence are not the best choice for sequential data processing. To handle such problems, a recurrent neural network (RNN) was introduced, which was specifically developed to address sequential data [41–43]. RNNs contain loops among the different nodes in their architecture to retain information in the model for long periods. RNNs employ the current input with the previous memory state. This ability of memory-keeping enables RNNs to predict what comes next. Furthermore, RNNs were designed to handle sequential data, which implies that updating the learnable weights must consider the extent of the time dimension. Accordingly, the backpropagation [44] algorithm responsible for updating the learnable weights needs some modification to work along with the time dimension. To alleviate this problem, backpropagation through time (BPTT) [41, 43] was introduced. Therefore, in basic RNNs, short-term memories are only preserved, so it becomes unfeasible in the case of dealing with long sequences of data. Therefore, basic RNNs usually suffer from issues like vanishing or exploding gradients in such situations [45]. Therefore, the fine-tuning of the model parameters and training of RNNs becomes very hard. To overcome such issues, Hochreiter and Schmidhuber developed the Long-Short Term Memory networks (LSTMs [46]).

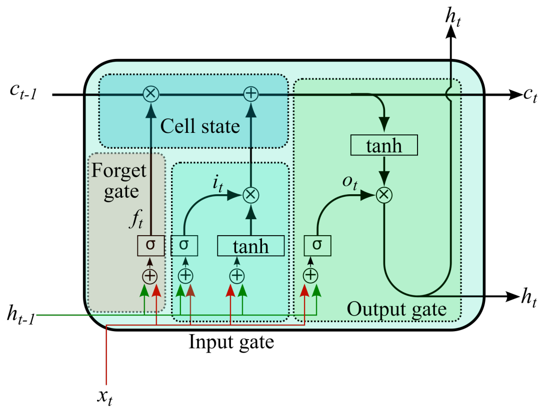

(a) LSTM

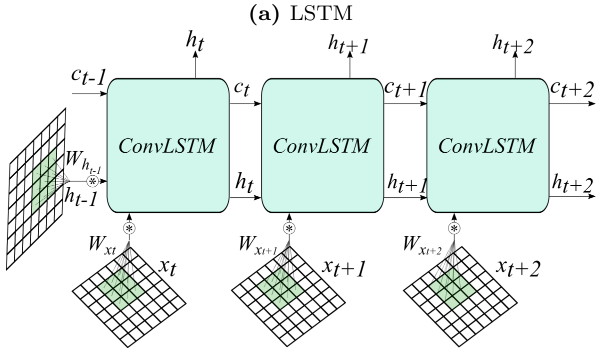

(b) ConvLSTM

Figure 4: LSTM and ConvLSTM architectures.

LSTMs were developed to keep information related to long-term dependencies and to solve the problem of vanishing and exploding gradients. Further, LSTMs handle inputs or outputs of any length, which makes LSTMs powerful for solving very complex sequential problems. Basic LSTM architecture shown in Fig. 4a consists of four units: an input gate, a cell state, a forget gate, and an output gate. These gates help regulate the flow of information that is added to or removed from the cell state. The hidden states in LSTM hold the short-term memory, while the cells state holds the long-term memory.

The purpose of the forget gate is to decide what information to keep and what to neglect. The current input x_t and the previous hidden state h_{t-1} are passed through a sigmoid function (σ) which produce values between 0 and 1. Then the outputs of the sigmoid are multiplied with the previous cell state $c_t - 1$. Consequently, (0) outputs are discarded. The mathematical calculation at the forget gate (f_t) is depicted in Eq. (1):

$$\begin{aligned} f_t &= \sigma\left(W_f \begin{bmatrix} h_{t-1} \\ x_t \end{bmatrix} + b_f\right) \\ W_f &= \left[W_{h_{t-1}} W_{x_t}\right] \end{aligned} \tag{1}$$

where W_f represent the learnable weights at the hidden and input states h_{t-1} and x_t, respectively, and b_f represents the bias term.

The input gate i_t takes the current input x_t with the previous hidden state h_{t-1}, then applies the sigmoid function to get values in a range between 0 (not important) and 1 (important). Then, the same current input x_t, and the hidden state h_{t-1} are passed through a tanh function at the cell state ($\tilde{c}_t$) that regulate the network by transferring the values into a range between -1 and 1. Then, the outputs from the sigmoid and tanh functions are multiplied point-by-point to eliminate 0 values. Eq. (2) depicts the calculation at the input gate:

$$\begin{aligned} i_t &= \sigma\left(W_i \begin{bmatrix} h_{t-1} \\ x_t \end{bmatrix} + b_i\right) \\ \tilde{c}_t &= \tanh\left(W_c \begin{bmatrix} h_{t-1} \\ x_t \end{bmatrix} + b_c\right) \end{aligned} \tag{2}$$

At this point, the network has sufficient information obtained from the input and forget gates. Hence, the current cell state c_t can be calculated by multiplying the previous cell state c_{t-1} with the output of the forget gate. Then, the result is added to the calculated input values as depicted in Eq. (3):

$$c_t = f_t \cdot c_{t-1} + i_t \cdot \tilde{c}_t \tag{3}$$

The output gate o_t computes the next hidden state h_t which holds information related to the current inputs. Accordingly, the current input x_t and the previous hidden state h_{t-1} are passed through a third sigmoid function to produce values between 0 and 1. The current cell state c_t is passed through a tanh function and multiplied point-by-point with o_t to produce the new hidden state h_t which is transferred to the next timestamp. Equation (4) illustrates the calculations at the output gate:

$$\begin{aligned} o_t &= \sigma\left(W_o \begin{bmatrix} h_{t-1} \\ x_t \end{bmatrix} + b_o\right) \\ h_t &= o_t \cdot \tanh\left(c_t\right) \end{aligned} \tag{4}$$

where W_f, W_i, W_c and W_o have shared learnable weights.

Recently, LSTMs have been widely used for large-scale learning of language translation models, speech recognition systems, chatbots, forecasting stock markets, text data analysis, and many more [47, 48]. However, LSTMs are inefficient at capturing spatial information by themselves when the time series inputs are consecutive images. Hence, the ConvLSTM architecture, which is a combination of CNN and LSTM units, was introduced by Shi et al. [49] to solve such kind of problems. In ConvLSTM, the convolution operations are applied both at the input-to-state transition and at the state-to-state transitions. The ConvLSTM unit, shown in Fig. 4b is a variation of the LSTM cell as it performs a convolution operation within the LSTM cell. ConvLSTM is a combination of a convolution operation and an LSTM cell. Thus, ConvLSTM can capture the time-correlated and spatial features in a series of consecutive images. Equation (5) depicts the ConvLSTM operations as the inputs $x_1, \ldots, x_t$, hidden states $h_1, \ldots, h_t$, cell states $c_1, \ldots, c_t$ and input, forget, and output gates are represented as i_t, f_t, and o_t, respectively:

$$\begin{aligned}
i_t &= \sigma\left(W_{x_t} * x_t + W_{h_{t-1}} * h_{t-1} + W_{ci} \cdot c_{t-1} + b_i\right) \\
f_t &= \sigma\left(W_{xf} * x_t + W_{hf} * h_{t-1} + W_{cf} \cdot c_{t-1} + b_f\right) \\
c_t &= f_t \cdot c_{t-1} + i_t \cdot \tanh\left(W_{xc} * x_t + W_{hc} * h_{t-1} + b_c\right) \\
o_t &= \sigma\left(W_{xo} * x_t + W_{ho} * h_{t-1} + W_{co} \cdot c_t + b_o\right) \\
h_t &= o_t \cdot \tanh\left(c_t\right)
\end{aligned} \tag{5}$$

where $(*)$ indicates the convolution operation, which is an element-wise multiplication operation.

Recently, ConvLSTM has become very popular and is increasingly being used in image processing applications.

5 The proposed model

In this work, the author developed an end-to-end deep learning model utilising full wavefield frames of Lamb wave propagation for delamination identification in CFRP materials. The developed model have a scheme of many-to-one sequence prediction, which takes m number of frames representing the full wavefield propagation through time and their interaction with the delamination to extract the damage features and finally predict the delamination location, shape, and size in a single output image.

The proposed model, presented in Fig. 5 takes 64 frames as input, and it consists of three ConvLSTM layers. The first ConvLSTM layer has 12 filters, the second layer has 6 filters, and the third layer has 12 filters. The kernel size of the ConvLSTM layers was set to (3×3) with a stride of (1). Padding was set to "same", which makes the output the same as the input in the case of stride 1. Furthermore, a tanh (the hyperbolic tangent) activation function was used within the ConvLSTM layers that output values in a range between (-1 and 1). Moreover, a batch normalization technique [50] was applied after the first two ConvLSTM layers.

At the final output layer, a 2D convolutional layer followed by a sigmoid activation function is applied that outputs values in a range from $(0, 1)$ to indicate the delamination probability. Consequently, a threshold value must be chosen to classify the output into damaged (represented by 1) or undamaged (represented by 0). Hence, the author set the threshold value to (0.5) to exclude all values below the threshold by considering them as undamaged and taking only those values greater than the threshold to be considered as damaged.

For evaluating the performance of the proposed model, the mean intersection over union IoU (Jaccard index) was applied as the accuracy metric. IoU is estimated by determining the intersection area between the ground truth and the predicted output.

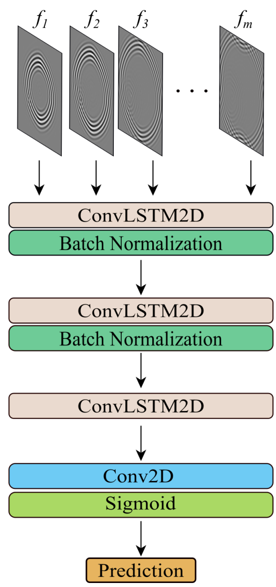

Figure 5: The architecture of the proposed deep learning model.

Further, there are two output classes (damaged and undamaged), the IoU was calculated for the damaged class only. Equation (6) illustrates the IoU metric:

$$IoU = \frac{Intersection}{Union} = \frac{\hat{Y} \cap Y}{\hat{Y} \cup Y} \tag{6}$$

where $\hat{Y}$ is the predicted output, and Y is the ground truth. Additionally, the percentage area error (ϵ) depicted in Eqn. 7 was utilised to evaluate the performance of the proposed model:

$$\epsilon = \frac{|A - \hat{A}|}{A} \times 100\% \tag{7}$$

where A and $\hat{A}$ refer to the area in mm^2 of the damage class in the ground truth and the predicted output, respectively. This metric can indicate how close the area of the predicted delamination is to the ground truth. Accordingly, the lower the value of (ϵ), the higher the accuracy of the identified damage. Furthermore, for all of the predicted outputs, the delamination localisation error (the distance between the delamination centres of the GT and the predicted output) was less than (0.001%), hence, it is not considered in the discussion section.

6 Results and discussions

In this section, the author presents the evaluation of the proposed model based on numerical data of 95 different cases representing the frames of the full wavefield propagation. The proposed model was evaluated using numerical and experimental data to demonstrate the capability to predict delamination location, shape, and size. Therefore, three representative cases were selected from the numerical dataset to show the performance of the developed model. For numerical cases, the predicted results were obtained by using only the first window of frames after the interaction with the damage, as the delamination ground truths are provided, which is not the case for real-life scenarios as in the experimental section. Consequently, the part of producing intermediate predictions and further calculating the RMS image was skipped.

To evaluate the generalisation capability of the developed model, experimental data of single and multiple delaminations were considered. The IoU metric was utilised to examine the performance of the model. Furthermore, the proposed deep learning model was implemented on Keras API [51] running on top of TensorFlow on a Tesla V100 GPU from NVIDIA.

6.1 Numerical cases

In the first numerical case, the delamination is located at the upper left corner, as shown in Fig. 6a, representing its ground truth (GT). This case is considered difficult due to edge wave reflections that have similar patterns as delamination reflection.

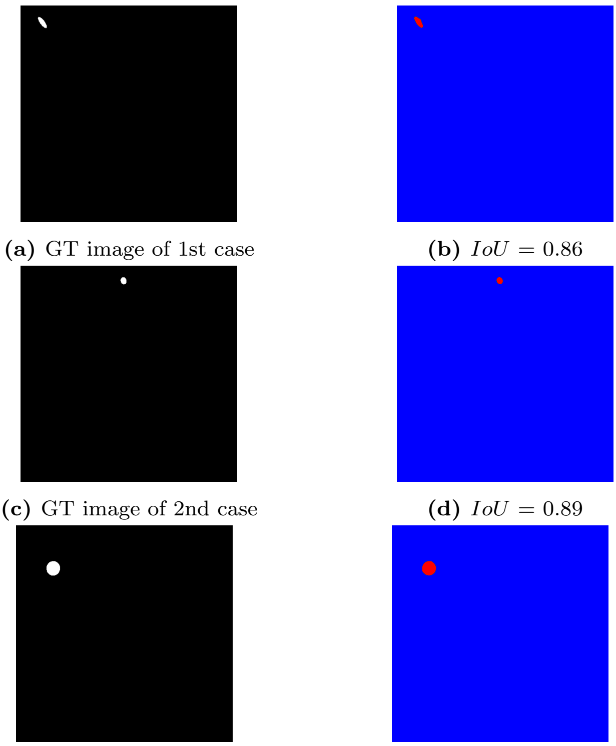

(a) GT image of 1st case **(b)** $IoU = 0.86$

(c) GT image of 2nd case **(d)** $IoU = 0.89$

(e) GT image of 3rd case **(f)** $IoU = 0.98$

Figure 6: Delamination cases on numerical data (Figures: (a), (c), and (e) correspond to the GT of each numerical case. Figures: (b), (d) and (f) correspond to the predictions of the proposed model).

The predicted output of the first numerical case is shown in Fig. 6b. For the second numerical case, the delamination is located at the upper centre of the plate, as shown in Fig. 6c, representing the GT. This case is considered difficult due to the waves reflected from the edge have similar patterns to those reflected from the delamination. Fig. 6d shows the prediction of the second numerical case. In the third case, the delamination is located at the upper left corner but a little farther from the edges, as shown in Fig. 6e, representing the GT. Fig. 6f shows the predicted output of the model. As can be seen in all predicted outputs, the proposed model is able to identify the delamination with high accuracy and without any noise.

Tab. 1 presents the evaluation metric of the proposed model, regarding the numerical cases shown in Fig. 6. As shown in Tab. 1, the actual (A) and predicted areas ($\hat{A}$) of delaminations were computed in mm^2 with respect to each case. The percentage area error (ϵ) was also calculated for the proposed model. The achieved mean IoU with respect to all numerical data of 95 cases was (0.90). Furthermore, the mean percentage area error (ϵ) was calculated for all numerical cases (95) was equal to 4.57%.

Table 1: Evaluation metric of the three numerical cases

Case number	**A [mm^2]**	**IoU**	$\hat{A}$ **[mm^2]**	ϵ
1	272	0.86	318	16.9%
2	186	0.89	196	5.4%
3	842	0.98	871	3.4%

6.2 Experimental cases

In this section, the author investigated the proposed model using experimentally acquired data. Similarly to the synthetic dataset, a frequency of 50 kHz is applied to excite a signal in a transducer placed at the centre of the plate. $A0$ mode wavelength for this particular CFRP material at such frequency is 19.5 mm. The measurements were performed by using Polytec PSV-400 SLDV on the bottom surface of the plate with dimensions of 500 × 500 mm. The measurements were conducted on a regular grid of 333×333 points. The measurement area was aligned with the plate edges. The sampling frequency was 512 kHz. To improve the signal-to-noise ratio, 10 averages were used. The total scanning time for one specimen was about 1h 40'. Further, a median filter using a window size of three was applied to each frame. Additionally, all frames were upsampled by using cubic interpolation to 500 × 500 points.

During the testing stage of the synthetic dataset, the model was fed with a consecutive number of identified frames (window of frames) containing the interactions of the Lamb waves with the delamination to identify it.

6.3 Single delamination

The first experimental case is for a CFRP specimen with single delamination created artificially by a Teflon insert of a thickness 250 μm. The complete specifications of this CFRP specimen is similar to the numerical investigations. A plain weave fabric reinforcement was used. The Teflon of a square shape was inserted during specimen manufacturing, so its shape and location are known. Based on that, the ground truth was prepared manually. Fig. 7a shows the GT image which corresponds to the artificial delamination location, shape and size. The number of the full wavefield frames is 256 frames in this case. Fig 7b shows the delamination prediction for the proposed model, and the highest IoU is (0.53) achieved for a group of frames ($35 - 99$).

Furthermore, the percentage area error metric (ϵ) was equal to 41.78%. Therefore, delamination was detected, located but its size was unidentified properly with mentioned error. The predictions were highest for the group of frames corresponding to the first interaction of the guided waves with the delamination. Accordingly, such frames contain the most valuable feature patterns regarding delamination.

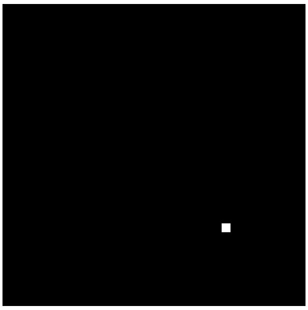

(a) GT of Teflon insert

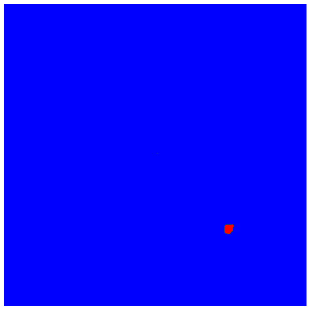

(b) $IoU = 0.53$

Figure 7: Experimental case: single delamination of Teflon insert. (Figure (a) correspond to the GT of this experimental case. Figure (b) correspond to the predictions of the proposed model).

Furthermore, this behaviour can be depicted in Fig. 8, which shows the IoU values with respect to the predicted outputs as the author slide the window over all input frames from the starting frame till the end. Since there are 256 frames of full wavefield in this damage case, there are 192 frames of windows and has 192 consecutive predictions. Furthermore, in Fig. 8a, three places for the sliding window was selected. The first place depicted in a dark blue star shown in Fig. 8b represents a group of frames $(72-136)$ which correspond to the initial interaction of guided waves with the delamination. The second place is depicted in the pink pentagon shape shown in Fig. 8b represents a group of frames $(129-193)$ that correspond to the guided waves reflected from the edges, in which the drop in the IoU values can be noticed as these frames have fewer damage features. The third place, depicted in the green circle shown in Fig. 8b represents a group of frames $(192-256)$ corresponding to the interaction of the guided waves reflected from the edges with the delamination. As it can be seen, the value of IoU increases again as the valuable feature patterns regarding delamination start to appear again. The predicted outputs of the proposed model regarding the dark blue star, pink pentagon, and the green circle are shown in Fig. 9.

Additionally, for the experimental cases, the author applied the root mean square (RMS) according to Eq. 8 for all N predicted outputs $\hat{Y}$ regarding all windows of frames in order to show the damage map.

$$RMS = \sqrt{\frac{1}{N}\sum_{k=1}^{N}\hat{Y}^2} \tag{8}$$

To separate damaged and undamaged classes from the RMS images, a binary threshold with a value ($threshold = 0.5$) is applied as shown in Fig. 10a. The threshold level was selected to limit the influence of noise and at the same time highlight the damage. Fig. 10b shows the RMS image for the experimental case of single delamination predicted by the proposed model. The calculated IoU value for the case of single delamination was (0.46).

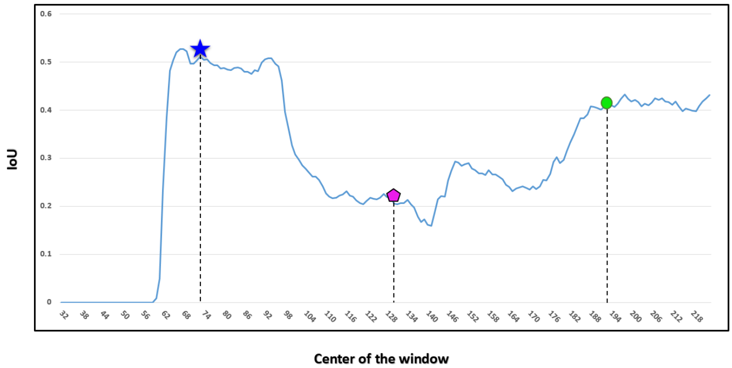

(a) IoU for the sliding window centered at consecutive frames.

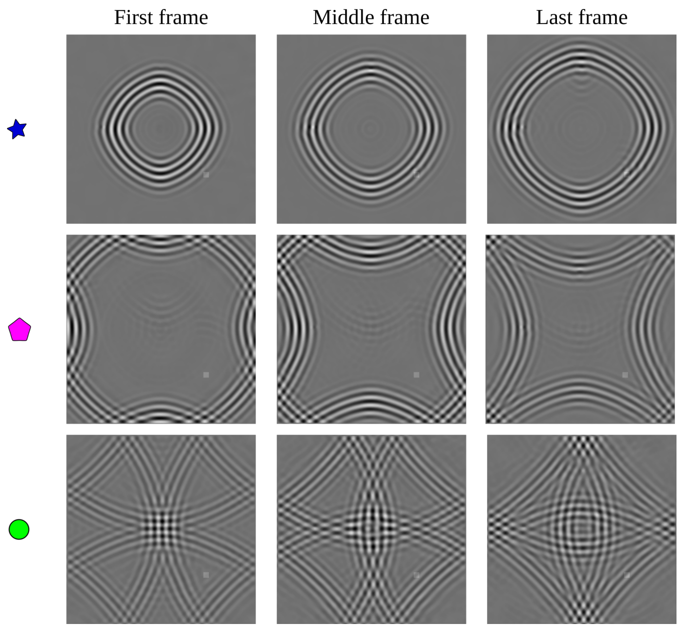

(b) Corresponding frames of guided waves.

Figure 8: IoU corresponding to a sliding window of frames (Teflon insert-single delamination).

Tab. 2 presents the evaluation metric for the proposed model, regarding the experimental case of single delamination shown in Fig. 10. As shown in Tab. 2, the actual (A) and predicted areas ($\hat{A}$) of delaminations were computed in [mm^2] with respect to each case and the percentage area error (ϵ) was calculated.

Table 2: Evaluation metric for experimental case of single delamination

Experimental case	**A [mm^2]**	**IoU**	$\hat{A}$ **[mm^2]**	ϵ
Single delamination	255	0.46	319	41.78%

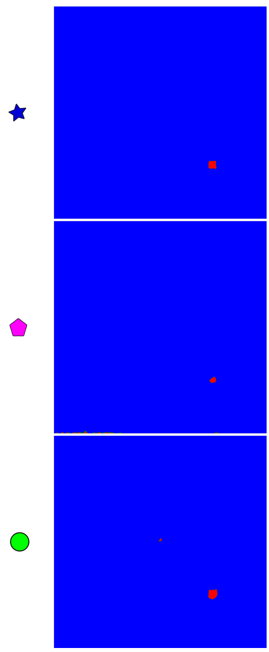

Figure 9: Predictions of the proposed model at different window places (Teflon insert-single delamination).

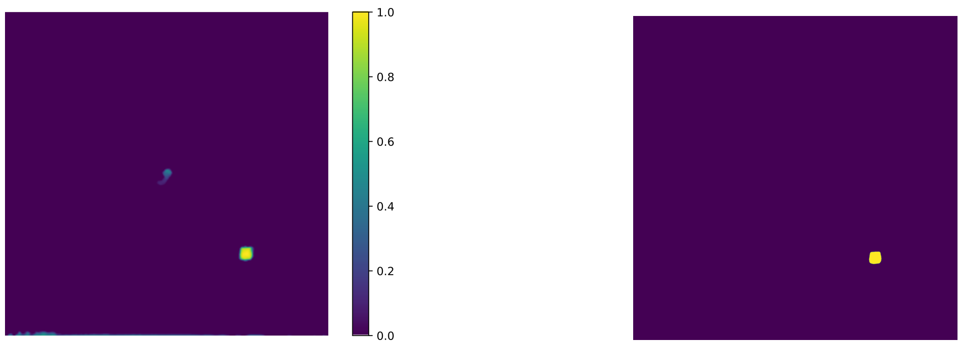

(a) **(b)**

Figure 10: RMS and thresholded RMS images of predicted outputs -Teflon insert (single delamination): (a) RMS image of predicted output, (b) Thresholded RMS image of predicted output ($IoU = 0.46$)

6.4 Multiple delaminations

In the second experimental case, the author investigated three specimens of carbon/epoxy laminate reinforced by stacking sequence of 16 layers of plain weave fabric as shown in Fig. 11. Teflon inserts with a thickness of 250 μm) were used to simulate the delaminations. The prepregs GG 205 P (fibres Toray FT 300–3K 200 tex) by G. Angeloni and epoxy resin IMP503Z-HT by Impregnatex Compositi were used for the fabrication of the specimen in the autoclave. The average thickness of the specimen was 3.9 mm.

In Specimen 2, three large artificial delaminations of elliptic shape were inserted in the upper thickness quarter of the plate between the 4^{th} and the 5^{th} layer. The delaminations were located at the same distance, equal to 150 mm from the centre of the plate. For Specimen 3, delaminations were inserted in the middle thickness of the plate between 8^{th} layer and 9^{th} layer. For Specimen 4, three small delaminations were inserted in the middle of the thickness of the plate, and three large delaminations were inserted at the lower quarter of the thickness of the plate between the 12^{th} layer and 13^{th} layer. The details of Specimen 2, 3 and 4 are presented in Fig. 11.

Furthermore, the SLDV measurements were conducted from the bottom surface of the plate. Consequently, Specimen 2 is the most difficult case, as the delaminations are barely visible. For Specimens (2, 3, and 4), 512 consecutive frames were generated representing the full wavefield measurements in the plate. The measurement parameters were the same as in the experiment with single delamination. Since SLDV measurements

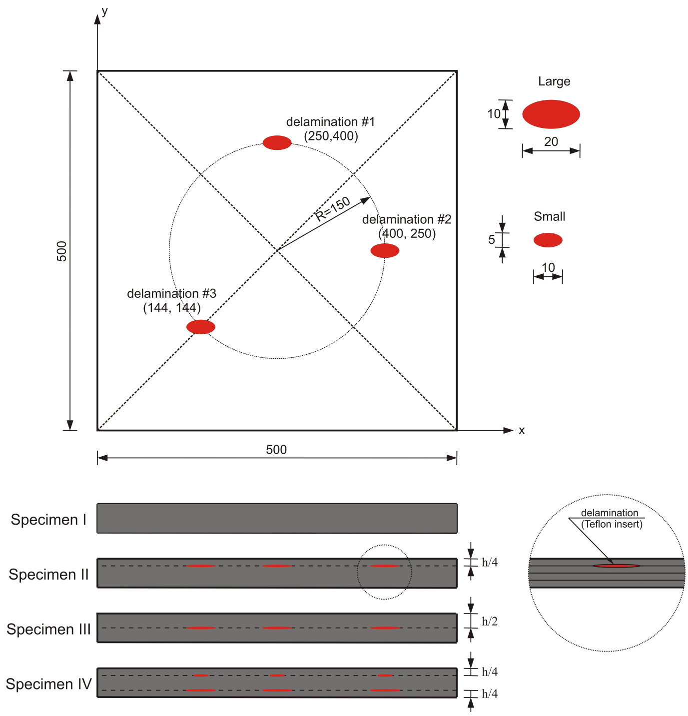

Figure 11: Experimental case of delamination arrangement.

were conducted from the bottom surface of the plate, the GT images and the output predictions of the proposed model are flipped horizontally (mirrored). Fig. 12a shows the GT image of Specimen 2. The predicted output of the proposed model is shown in Fig. 12b in which the highest calculated IoU value is 0.15 achieved for the group of frames $(167-231)$. Figure 12c shows the GT image of Specimen 3. The predicted output is shown in Fig. 12d in which the highest calculated IoU value is 0.18 achieved for group of frames $(279-343)$.

Fig. 12e shows the GT image of Specimen 4. This is assumed to be the largest delaminations in the cross-sections because the full wavefield was acquired from the bottom surface of the specimen. It is also to be noted that such a case with stacked delaminations in cross-sections was not modeled numerically (see Specimen 4 in Fig. 11). Although the model was not trained on such a scenario, the predictions were satisfactory. The predicted

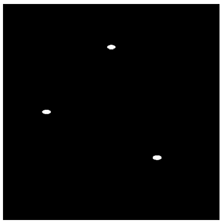

(a) GT of Specimen 2

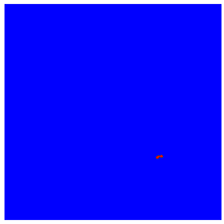

(b) IoU = 0.15

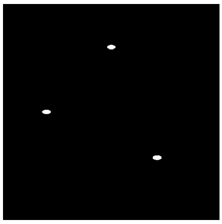

(c) GT of Specimen 3

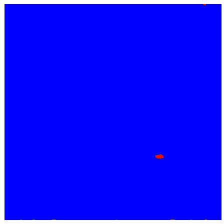

(d) IoU = 0.18

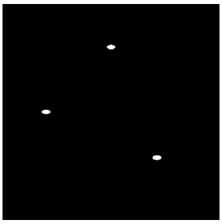

(e) GT of Specimen 4

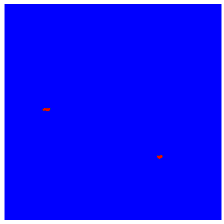

(f) IoU = 0.18

Figure 12: Experimental cases of Specimens 2, 3, and 4. (Figures: (a), (c), and (e) correspond to the GT of each Specimen. Figures: (b), (d) and (f) correspond to the predictions of the proposed model).

output of the proposed system is shown in Fig. 12f in which the highest calculated IoU value is 0.18 achieved for the group of frames $(235 - 299)$.

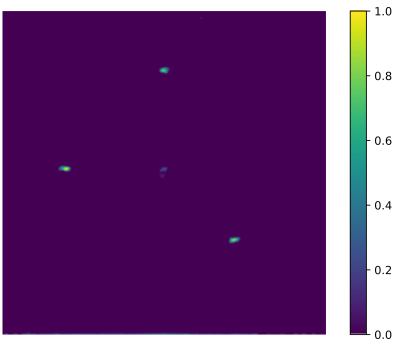

(a)

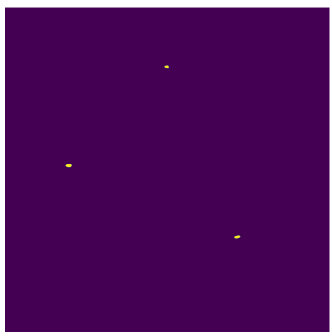

(b)

Figure 13: RMS and Thresholded RMS images of predicted outputs - Specimen 4: (a) RMS image of the predicted output, (b) Thresholded RMS image of predicted output (IoU = 0.07).

The RMS images depicting the damage maps of Specimen 4 are presented in Fig. 13a for the proposed model. Fig. 13b shows the thresholded RMS image for the proposed model, and the calculated value of IoU is (0.07). Furthermore, the mean percentage area error (ϵ) with respect to the three delaminations (Specimen 4) for the proposed model was equal to 79.41%.

7 Conclusions

In this work, the author presented a novel deep learning-based approach for delamination identification in composite laminates. The developed approach introduces an end-to-end scheme that performs a many-to-one sequence prediction to identify delamination location, size, and shape. Accordingly, the proposed model is trained on a consecutive number of frames depicting the full wavefield of Lamb waves propagation in a plate of CFRP, and their interactions with the delamination, and the edges. Hence, the proposed model learn how to extract the valuable features regarding the damage from such frames in order to have a prediction.

To evaluate the performance of the developed model, the author examined them on a numerical test-set that was unseen before. The results verified their ability to identify the delaminations with high accuracy. Furthermore, to evaluate the generalisation capability of the proposed model, the author tested it on several experimentally measured cases of single and multiple delaminations simulated by Teflon inserts. The predicted results are promising, considering the experimental case of multiple delaminations is difficult as the model was trained only on cases of single delamination. Consequently, the currently developed model showed its potential capability of identifying multiple delaminations at once in real-life cases.

However, there are several limitations to the SLDV measurement technique, which is used for full wavefield acquisition. The measurements constructed by using SLDV are stationary and time-consuming. Therefore, the proposed technique is more appropriate for NDT than SHM. However, it is probable that in the future, as laser technology progresses, the process of data acquisition will be possible at an array of points instead of a single point, which will considerably decrease the measurement time. It is also possible that the measurement time can be reduced by using fewer points in the spatial grid along with the compressive sensing approach. Another issue with SLDV measurements is that the laser needs access to the surface of the inspected structure, which may require partial disassembly of the structure.

The limitation related to the developed deep learning model is that the material properties of the inspected structure have to be approximately known in order to simulate the dataset for training.

Acknowledgements

The research was funded by the Polish National Science Center under grant agreement no 2018/31/B/ST8/00454.

Received in February 2022

References

[1] V. Giurgiutiu, "Structural health monitoring (SHM) of aerospace composites," *Polymer Composites in the Aerospace Industry*, pp. 491–558, 2019.

[2] F. Xu, Q. D. Duan Mu, L. J. Li, D. Yang, and B. Xia, "Nondestructive evaluation of rubber composites using terahertz time domain spectroscopy," *Fibres and Textiles in Eastern Europe*, vol. 26, no. 1, pp. 67–72, 2018.

[3] A. Poudel, S. S. Shrestha, J. S. Sandhu, T. P. Chu, and C. G. Pergantis, "Comparison and analysis of Acoustography with other NDE techniques for foreign object inclusion detection in graphite epoxy composites," *Composites Part B: Engineering*, vol. 78, pp. 86–94, sep 2015.

[4] R. Talreja and C. V. Singh, *Damage and failure of composite materials.* Cambridge University Press, 2012.

[5] M. R. Wisnom, "The role of delamination in failure of fibre-reinforced composites," *Philosophical Transactions of the Royal Society A: Mathematical, Physical and Engineering Sciences*, vol. 370, no. 1965, pp. 1850–1870, 2012.

[6] W. J. Staszewski, S. Mahzan, and R. Traynor, "Health monitoring of aerospace composite structures - Active and passive approach," *Composites Science and Technology*, vol. 69, no. 11-12, pp. 1678–1685, 2009.

[7] H. Tuo, Z. Lu, X. Ma, J. Xing, and C. Zhang, "Damage and failure mechanism of thin composite laminates under low-velocity impact and compression-after-impact loading conditions," *Composites Part B: Engineering*, vol. 163, pp. 642–654, 2019.

[8] R. J. Barthorpe and K. Worden, "Emerging Trends in Optimal Structural Health Monitoring System Design: From Sensor Placement to System Evaluation," *Journal of Sensor and Actuator Networks 2020, Vol. 9, Page 31*, vol. 9, p. 31, jul 2020.

[9] J. B. Ihn and F. K. Chang, "Pitch-catch active sensing methods in structural health monitoring for aircraft structures," *Structural Health Monitoring*, vol. 7, pp. 5–19, mar 2008.

[10] S. Cantero-Chinchilla, J. Chiachío, M. Chiachío, D. Chronopoulos, and A. Jones, "Optimal sensor configuration for ultrasonic guided-wave inspection based on value of information," 2020.

[11] M. Radzieński, P. Kudela, A. Marzani, L. De Marchi, and W. Ostachowicz, "Damage identification in various types of composite plates using guided waves excited by a piezoelectric transducer and measured by a laser vibrometer," *Sensors (Switzerland)*, vol. 19, p. 1958, apr 2019.

[12] D. Girolamo, H. Y. Chang, and F. G. Yuan, "Impact damage visualization in a honeycomb composite panel through laser inspection using zero-lag cross-correlation imaging condition," *Ultrasonics*, vol. 87, pp. 152–165, jul 2018.

[13] P. Kudela, M. Radzienski, and W. Ostachowicz, "Impact induced damage assessment by means of Lamb wave image processing," *Mechanical Systems and Signal Processing*, vol. 102, pp. 23–36, mar 2018.

[14] M. D. Rogge and C. A. Leckey, "Characterization of impact damage in composite laminates using guided wavefield imaging and local wavenumber domain analysis," *Ultrasonics*, vol. 53, no. 7, pp. 1217–1226, 2013.

[15] S. P. Mohanty, D. P. Hughes, and M. Salathé, "Using Deep Learning for Image-Based Plant Disease Detection," *Frontiers in Plant Science*, vol. 7, p. 1419, sep 2016.

[16] X. Zhang, L. Han, L. Han, and L. Zhu, "How Well Do Deep Learning-Based Methods for Land Cover Classification and Object Detection Perform on High Resolution Remote Sensing Imagery?," *Remote Sensing*, vol. 12, p. 417, jan 2020.

[17] M. Pashaei, H. Kamangir, M. J. Starek, and P. Tissot, "Review and Evaluation of Deep Learning Architectures for Efficient Land Cover Mapping with UAS Hyper-Spatial Imagery: A Case Study Over a Wetland," *Remote Sensing*, vol. 12, p. 959, mar 2020.

[18] R. Zhao, R. Yan, Z. Chen, K. Mao, P. Wang, and R. X. Gao, "Deep learning and its applications to machine health monitoring," *Mechanical Systems and Signal Processing*, vol. 115, pp. 213–237, 2019.

[19] D. Chakraborty, "Artificial neural network based delamination prediction in laminated composites," *Materials and Design*, vol. 26, no. 1, pp. 1–7, 2005.

[20] A. Khan, D. K. Ko, S. C. Lim, and H. S. Kim, "Structural vibration-based classification and prediction of delamination in smart composite laminates using deep learning neural network," *Composites Part B: Engineering*, vol. 161, no. August 2018, pp. 586–594, 2019.

[21] Q. Luo, B. Gao, W. L. Woo, and Y. Yang, "Temporal and spatial deep learning network for infrared thermal defect detection," *NDT & E International*, vol. 108, p. 102164, 2019.

[22] H.-T. Bang, S. Park, and H. Jeon, "Defect identification in composite materials via thermography and deep learning techniques," *Composite Structures*, vol. 246, p. 112405, 2020.

[23] Z. Su and L. Ye, "Lamb wave-based quantitative identification of delamination in CF/EP composite structures using artificial neural algorithm," *Composite Structures*, vol. 66, pp. 627–637, oct 2004.

[24] D. Chetwynd, F. Mustapha, K. Worden, J. A. Rongong, S. G. Pierce, and J. M. Dulieu-barton, "Damage localisation in a stiffened composite panel," *Strain*, vol. 44, no. 4, pp. 298–307, 2008.

[25] A. De Fenza, A. Sorrentino, and P. Vitiello, "Application of Artificial Neural Networks and Probability Ellipse methods for damage detection using Lamb waves," *Composite Structures*, vol. 133, pp. 390–403, 2015.

[26] B. Feng, D. J. Pasadas, A. L. Ribeiro, and H. G. Ramos, "Locating Defects in Anisotropic CFRP Plates Using ToF-Based Probability Matrix and Neural Networks," *IEEE Transactions on Instrumentation and Measurement*, vol. 68, no. 5, pp. 1252–1260, 2019.

[27] A. Mardanshahi, V. Nasir, S. Kazemirad, and M. M. Shokrieh, "Detection and classification of matrix cracking in laminated composites using guided wave propagation and artificial neural networks," *Composite Structures*, vol. 246, p. 112403, 2020.

[28] C. Qian, Y. Ran, J. He, Y. Ren, B. Sun, W. Zhang, and R. Wang, "Application of artificial neural networks for quantitative damage detection in unidirectional composite structures based on Lamb waves," *Advances in Mechanical Engineering*, vol. 12, no. 3, p. 1687814020914732, 2020.

[29] I. Tabian, H. Fu, and Z. S. Khodaei, "A convolutional neural network for impact detection and characterization of complex composite structures," *Sensors (Switzerland)*, vol. 19, no. 22, pp. 1–25, 2019.

[30] M. Rautela and S. Gopalakrishnan, "Ultrasonic guided wave based structural damage detection and localization using model assisted convolutional and recurrent neural networks," *Expert Systems with Applications*, vol. 167, p. 114189, 2021.

[31] G. Ros, L. Sellart, J. Materzynska, D. Vazquez, and A. M. Lopez, "The SYNTHIA Dataset: A Large Collection of Synthetic Images for Semantic Segmentation of Urban Scenes," in *Proceedings of the IEEE Computer Society Conference on Computer Vision and Pattern Recognition*, vol. 2016-Decem, pp. 3234–3243, Packt Publishing, 2016.

[32] W. Xu, B. Li, S. Liu, and W. Qiu, "Real-time object detection and semantic segmentation for autonomous driving," in *MIPPR 2017: Automatic Target Recognition and Navigation*, vol. 10608, p. 44, International Society for Optics and Photonics, Packt Publishing, 2018.

[33] S. A. Taghanaki, K. Abhishek, J. P. Cohen, J. Cohen-Adad, and G. Hamarneh, "Deep semantic segmentation of natural and medical images: a review," *Artificial Intelligence Review*, vol. 54, no. 1, pp. 137–178, 2021.

[34] A. Milioto, P. Lottes, and C. Stachniss, "Real-Time Semantic Segmentation of Crop and Weed for Precision Agriculture Robots Leveraging Background Knowledge in CNNs," in *Proceedings - IEEE International Conference on Robotics and Automation*, pp. 2229–2235, IEEE, Packt Publishing, 2018.

[35] O. Miksik, V. Vineet, M. Lidegaard, R. Prasaath, M. Nießner, S. Golodetz, S. L. Hicks, P. Pérez, S. Izadi, and P. H. Torr, "The semantic paintbrush: Interactive 3D mapping and recognition in large outdoor spaces," in *Conference on Human Factors in Computing Systems - Proceedings*, vol. 2015-April, pp. 3317–3326, Packt Publishing, 2015.

[36] R. Szeliski, *Computer vision: algorithms and applications.* Packt Publishing, 2010.

[37] S. Minaee, Y. Y. Boykov, F. Porikli, A. J. Plaza, N. Kehtarnavaz, and D. Terzopoulos, "Image segmentation using deep learning: A survey," *IEEE Transactions on Pattern Analysis and Machine Intelligence*, 2021.

[38] S. Ghosh, N. Das, I. Das, and U. Maulik, "Understanding deep learning techniques for image segmentation," *ACM Computing Surveys*, vol. 52, no. 4, pp. 1–35, 2019.

[39] P. Kudela, J. Moll, and P. Fiborek, "Parallel spectral element method for guided wave based structural health monitoring," *Smart Materials and Structures*, vol. 29, p. 095010, sep 2020.

[40] P. Kudela and A. Ijjeh, "Synthetic dataset of a full wavefield representing the propagation of Lamb waves and their interactions with delaminations," 2021.

[41] C. C. Aggarwal and Others, "Neural networks and deep learning," *Springer*, vol. 10, pp. 973–978, 2018.

[42] Y. LeCun, Y. Bengio, and G. Hinton, "Deep learning.," *Nature*, vol. 521, pp. 436–44, may 2015.

[43] I. G. Courville, Y. Bengio, and Aaron, *Deep learning*, vol. 29. MIT press Massachusetts, USA:, 2016.

[44] D. E. Rumelhart, G. E. Hinton, and R. J. Williams, "Learning representations by back-propagating errors," *Nature*, vol. 323, no. 6088, pp. 533–536, 1986.

[45] Y. Bengio, P. Simard, and P. Frasconi, "Learning long-term dependencies with gradient descent is difficult," *IEEE transactions on neural networks*, vol. 5, no. 2, pp. 157–166, 1994.

[46] S. Hochreiter and J. Schmidhuber, "Long Short-Term Memory," *Neural Computation*, vol. 9, pp. 1735–1780, nov 1997.

[47] A. Graves and N. Jaitly, "Towards end-to-end speech recognition with recurrent neural networks," in *International conference on machine learning*, pp. 1764–1772, PMLR, 2014.

[48] K. Cho, B. Van Merriënboer, D. Bahdanau, and Y. Bengio, "On the properties of neural machine translation: Encoder-decoder approaches," *arXiv preprint arXiv:1409.1259*, 2014.

[49] S. H. I. Xingjian, Z. Chen, H. Wang, D.-Y. Yeung, W.-K. Wong, and W.-c. Woo, "Convolutional LSTM network: A machine learning approach for precipitation nowcasting," in *Advances in neural information processing systems*, pp. 802–810, 2015.

[50] S. Santurkar, D. Tsipras, A. Ilyas, and A. Madry, "How does batch normalization help optimization?," in *Advances in Neural Information Processing Systems*, vol. 2018-Decem, pp. 2483–2493, 2018.

[51] F. Chollet, "Keras," 2015.

Development of thermal runaway emissions aftertreatment system (TREAS) of lithium ion batteries

Daniel Darnikowski*[1,2]

[1] *Maritime Advanced Research Centre, Szczecińska 65, 80-392 Gdańsk, Poland*
[2] *Institute of Fluid-Flow Machinery, Polish Academy of Sciences*
14 Fiszera Street, 80-231, Gdansk, Poland

Abstract

Lithium-ion batteries are one of the most cost effective portable energy containers. The fire incident involving such battery (often referred as "thermal runaway"), however, poses a great danger to the surrounding, particularly in the matter of emitted substances and their toxicity for human body. The substances found are carbon monoxide and dioxide, hydrogen and hydrogen fluoride. Filtration of these substances may be achieved with dry sorbent injection method, which uses calcium hydroxide. Dry injection filtering prototype is manufactured and tested against thermal runaway of the NCM cells. Following parameters are analysed: air flow, sorbet transport, air temperature of the flue gas and concentrations of the substances. Estimated filtering performance of the dry sorbent injection and air dilution at a flow rate of 1600 m^3/h and dosage of 1.8 g/s of calcium hydroxide is 99% for HF and 89% for CO_2. NMC cell gas production per Wh were respectively 1060.3 mg of CO_2 and 11.8 mg of H_2. Air speed of above 5 m/s was found sufficient to transfer the sorbent power from the hopper's inlet.

Keywords: lithium-ion, after-treatment, thermal runaway, emissions, LIB

1 Introduction

Lithium-ion batteries (LIB) are an enormous achievement in terms of technical and commercial side. LIB allows a vast scale of applications ranging from the cellphones to the large scale battery energy storage systems. Simultaneously, the fire caused by lithium-ion batteries are of a great concern, due to intense heat production as well as emissions of toxic gases [1–5]. Heat generated by the fire is a serious threat itself, however, toxic fumes may be even of a greater consideration, especially in a confined spaces such as closed rooms, underground parking spaces, spacecrafts, airplanes and other.

The fire incident of lithium-ion battery is caused by the event called "thermal runaway". Thermal runaway is a process that is accelerated by increased temperature, in turn releasing energy that further increases temperature [6]. In terms of lithium-ion battery (LIB), one or multiple cells start releasing internal energy in form of heat, which

*Corresponding Author. Email address: daniel.darnikowski@cto.gda.pl
https://doi.org/10.58139/v2q1-r455

is then transferred to another cells and modules causing a cascading effect [7, 8]. The initiation of the thermal runaway can have different causes - they are usually divided into three sources - mechanical abuse - such as in a crash, thermal abuse - e.g. overheating of the batteries or exposure to external source of heat or electrical abuse - e.g. overcharging. Summary of thermal runway mechanism has been shown in Fig. 1.

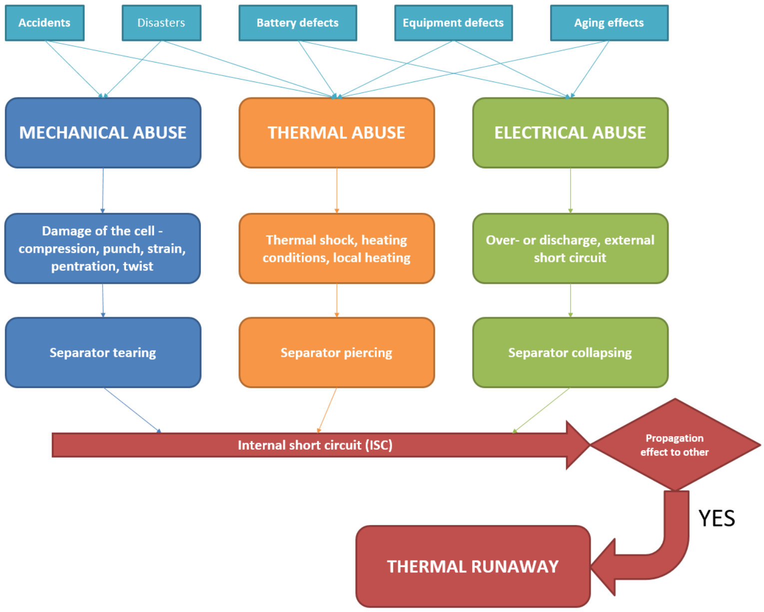

Figure 1: Battery safety issues. First row represents potential causes for LIB abuse. Second row divides given incident due to type of the abuse. Third row presents the examples of the processes causing given abuse to which LIBs are subjected. Fourth row presents damage to separator, which then results in internal short circuit [9]

.

Thermal runaway poses great challenge to the fire fighting brigades due to their self-sustaining nature [10], enclosures of the batteries inhibiting an easy pass of the cooling agent, toxic gaseous emissions [11] and heat generation [12]. The battery cannot be doused with conventional methods, as the battery is able to produce the oxygen by itself [11]. Instead, a lithium-ion battery is extinguished usually with the combination of state-of-art technology allowing to penetrate the enclosure battery with the cooling agents and then to drop the temperature below the critical point [13].

Since lithium-ion batteries cause severe incidents, which are difficult to control, they must undertake series of abuse tests before their introduction to the market [9, 14]. Type approval tests differ depending on geographical location of their the approving body [15], however, tests concerning fire resistance or exposure to high temperature usually cause test specimen to undergo thermal runaway event, producing vast amount of toxic compounds such as hydrogen fluoride, carbon monoxide, hydrogen, benzine and other cancerous aromatic compounds [16] and greenhouse gases [1]. Testing procedures such as GTR 20:2018 [17] (China), UNECE R100.02:2013 [18] (Europe), UNECE R100.03:2021 [19], ISO 12405-3:2014 [20] (global), ISO 6469-1:2019 [21] (global), ISO 18243:2017 [22] (global), SAE J2464:2009 [23] (North America), GB/T 31467.3-

2015 [24] (China), SAND2017-6925:2017 [25] (North America) and UL 2580:2020 [26] (North America) either deliberately cause thermal runaway to test against any signs of explosion of the cell, module or battery pack or use external heat source (petrol) to induce it.

Due to the fact there is little provided data on the methods of cleaning the toxic gases coming from the thermal runaway of the lithium-ion batteries, this paper describes the development of such prototype device together with the review of the compounds found in emitted gases, chemical and mechanical modelling of the device and test results containing air flow measurements and chemical analysis.

2 Thermal runaway emissions of lithium-ion batteries

Thermal runaway is preceded by the increase of temperature of the lithium-ion cell. First step is a breakdown of SEI layer (solid electrolyte interphase layer), layered on the anode. SEI layer purpose is to protect the anode from further reacting with the electrolyte [27]. The breakdown of the thin SEI layer occurs at 90-120°C, producing primarily CO_2 [28]:

$$(CH_2OCO_2Li)_2 \longrightarrow Li_2CO_3 + C_2H_4 + CO_2 + \tfrac{1}{2}\, O_2$$

Subsequently, due to SEI layer decomposition anode and electrolyte start to interact. Typical electrolytes found in lithium-ion batteries and their reaction with anode form flammable hydrocarbons are shown below [29]:

$$\begin{aligned}
&2\,Li + C_3H_4O_3\,(EC) \longrightarrow Li_2CO_3 + C_2H_4\\
&2\,Li + C_4H_6O_3\,(PC) \longrightarrow Li_2CO_3 + C_3H_6\\
&2\,Li + C_3H_6O_3\,(DMC) \longrightarrow Li_2CO_3 + C_2H_6
\end{aligned}$$

Subsequently, polyethylene or polypropylene separator melts at 135°C and 166°C respectively, and ceramic coated separator is found to maintain integrity even over 200°C [30]. As the temperature increase the separator shrinks until cathode and anode come into contact with each other to induce internal short circuit (ISC). ISC is a precursor for a thermal runaway, electric energy stored in the cell is further released in the approximately same amount [31].

Further reactions depend on the type of cathode used in the cell. These reaction mainly produce metallic oxides such as Co_3O_4 for LCO [32], LixCOyAlzOp for NCA, $(Mn, Ni)O$ and $Lix(Ni_{1/3}Co_{1/3}Mn_{1/3})O_2$ for NCM [33, 34] and other. Additionally, other by-products include oxygen and solid state metals.

Together with the cathode decomposition, electrolyte used in battery cell emits particular amount and type of toxic compounds. It is flammable and usually contains lithium hexafluorophosphate ($LiPF_6$) or other Li-based salts containing fluorine [35]. Promoted by the presence of water and humidity following reactions constitute to electrolyte decomposition [16]:

$$\begin{aligned}
&LiPF_6 \longrightarrow LiF + PF_6\\
&PF_5 + H_2O \longrightarrow POF_3 + 2\,HF\\
&LiPF_6 + H_2O \longrightarrow LiF + POF_3 + 2\,HF
\end{aligned}$$

The data has shown the production of HF and PO_3 per Wh at 100% SOC can be up to 193.3 mg and 22 mg respectively [16]. The production of other gaseous substances is dependent on the state of charge as well as type of chemistry used in the cell [36] and Fig. 2. Total gas generation is largely varying on used cathode material, state of charge of the cell and its shape. For the LCO/NCM 18650 type cell, it was found to be 265 mmol [37].

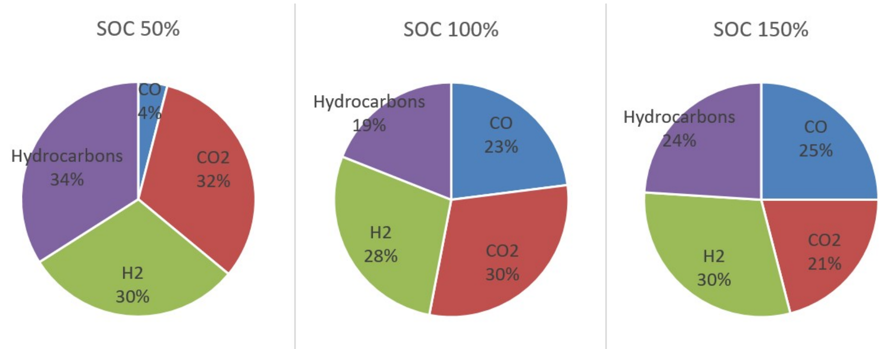

Figure 2: Composition of gases generated from thermal runaway of commercial LIBs. Somendepalli et al. [36] results of gas generated from 7.7 Wh LCO cell at different SOC.

3 Cleaning methods of the gas emissions

Toxic and acid gases, such as HCl, SO_2, CO_2, CO and HF can be neutralized by the designed agents, either supplied by the wet scrubbing equipment in absorbent solutions or by dry injection systems such as powdered alkaline sorbents [38]. Dry sorbent injection (DSI) systems characterise with low installed capital costs, relatively easy to retrofit to a majority of facilities, the system ensures good flexibility for various sorbents and low consumable requirements as well as parasitic power requirements to operate [39]. The two compounds have been predominantly used in the DSI - sodium or calcium-based [38, 40] - with the latter emerging as more accessible due to general availability of the limestone (calcium hydroxide) [41]. As such, calcium hydroxide was chosen for the TREAS to primarily clean hydrogen fluoride emissions.

After the calcium hydroxide is injected into gas emissions containing HF and CO_2 the following reactions can occur:

$$Ca(OH)_2 + 2\,HF \longrightarrow CaF_2 + H_2O$$

$$Ca(OH)_2 + CO_2 \longrightarrow CaCO_3 + H_2O$$

Thermodynamic calculations show the $CaCO_3$ and CaF_2 can only be formed at the temperatures below 600-800°C [42]. The products of reaction of the dry sorbent injection are then removed with mechanical filters (bag filters) and transposed to waste. The filter is intermittently cleaned with the jet pulse of air aimed. The schematics for the Thermal Runaway Emissions Aftertreatment System using dry sorbent injection are shown in Fig. 3.

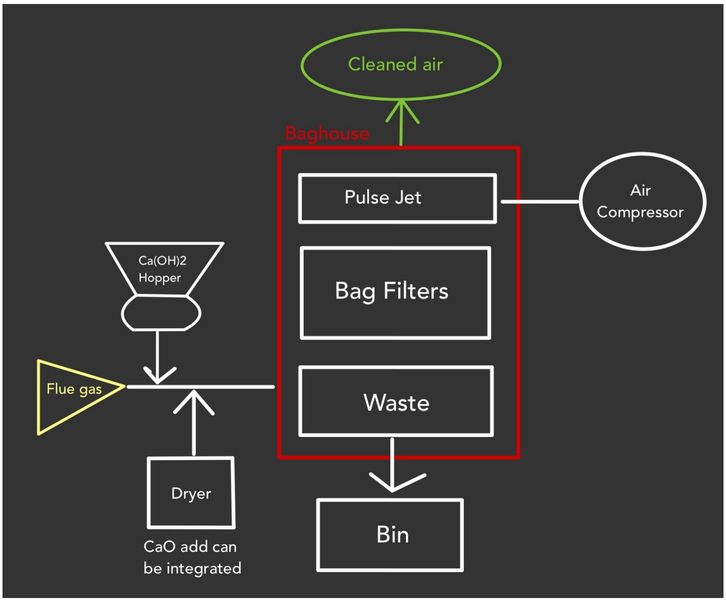

Figure 3: TREAS schematics using dry sorbent injection and calcium hydroxide. From right to left: flue gas is collected by the use of extraction hood, transported through the ventilation pipes to the baghouse. In midway the calcium hydroxide hopper supplies a dry sorbent in form of powder; dryer is optional. The bag house consists of mechanical filter (bag filter), air pulse jet (a nozzle to release compressed air for bag filter cleaning) and waste funnel (cone-shaped to limit the air leakage), below the baghouse a bin collects used dry sorbent agent. Other devices were air compressor for the pulse jet and fan for air flow with extraction of gases.

4 Development and test results of TREAS

Thermal Runaway Emissions Aftertreatment System was developed in stages with the optimisation of the air flow with the use of 3D modelling (Siemens NX), CFD computations (SOLIDWORKS Flow Simulation) and measurements on prototype and testing of thermal runaway NCM cells in various configurations. Next chapters present subsequent steps in TREAS development process.

The prototype is shown in Fig. 4.

4.1 Air flow simulations and measurements of the TREAS

The air flow in TREAS was simulated with SOLIDWORKS Flow Simulation CFD software. Nine TREAS 3D models were tested with various connectors and joints being used at 50°C and 300°C and with the fan performance of 1500 m^3/h. The model presumed the bottom outlet for the sorbent waste was closed for the sake of simulation simplicity. The overall pressure drops were respectively 300.9 Pa and 171.4 Pa for 50 and 300°C. The final model was shown in Fig. 5. The air flow before the filter bag were calculated to be at about 13 m/s, which were deemed optimal for the filtration purposes.

Figure 4: TREAS prototype testing site. P1, P2 and P3 probing points of the air flow. T1, T2, T3 temperature measurement points.

The measurement of the air flow was made on the TREAS prototype with the use of TESTO 480 anemometer and 0635 hot-wire probe. The probing was made in three locations shown in Fig. 4 and two fan performances (at 80% and 90%) for 30 min. and 1 Hz sampling:

- P1 - probing point after the fan.
- P2 - probing point before the filter.
- P3 - probing point at the extraction hood inlet.

The results of the flow measurement are shown in Fig. 6. The wind speed at the extraction hood inlet (P3) and before the filter (P2) is respectively 5 and 2-times lower than the simulated. It was found this is caused attributable to air leakages of the dosing system and waste removal. Simultaneously, the air flow was deemed sufficient to provide the transport and mixing of the dry sorbent, allow for periodical waste removal (jet-pulse), as well as limit the temperature of the thermal runaway gases, which may cause the filter to disintegrate. The wind speed at the fan exhaust was found similar to the simulated results.

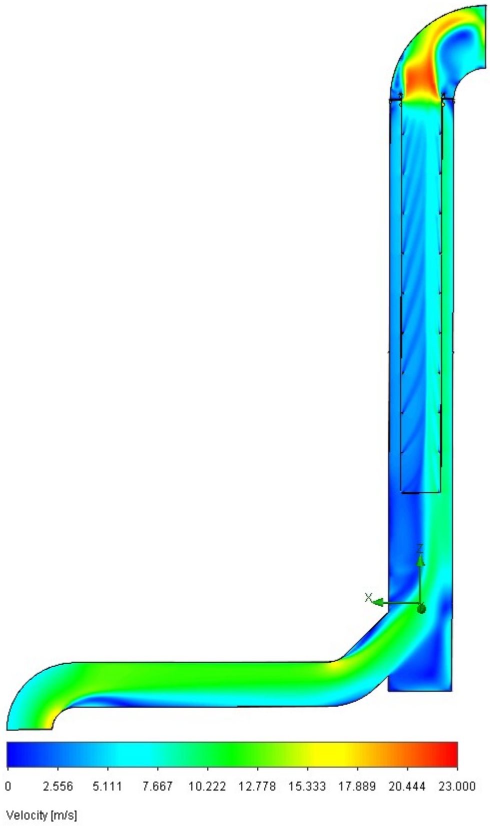

Figure 5: TREAS final model simulation at 50°C and 1500 m^3/h.

4.2 Thermal runaway tests

A series of tests were prepared to test the prototype performance in terms of gaseous composition (carbon dioxide, hydrogen and hydrogen fluoride) and temperature distribution inside TREAS. For the gas analysis a IR carbon dioxide sensor (resolution 0-100% v/v) and electrochemical sensors for hydrogen (resolution 0-40000 ppm v/v) and hydrogen fluoride (resolution 0-10 ppm v/v). Following configurations were tested two times each:

- Test Set-up 1: Thermal runaway of one NCM pouch battery cell (3.7 V, 60Ah, 220 Wh, 300x180x12 mm, 1120 g), fan power at 80%, sorbent dosage 1.8 g/s, pulse jet interval - 45 s break with 2 s air jet pulse.
- Test Set-up 2: Thermal runaway of two NCM pouch battery cell (3.7 V, 60Ah, 220 Wh, 300x180x12 mm, 1120 g), fan power at 90%, sorbent dosage 1.8 g/s, pulse jet interval - 45 s break with 2 s air jet pulse.
- Test Set-up 3: Thermal runaway of one NCM pouch battery cell (3.7 V, 60Ah, 220 Wh, 300x180x12 mm, 1120 g), fan power at 80%, sorbent dosage 0 g/s, pulse jet interval - off.

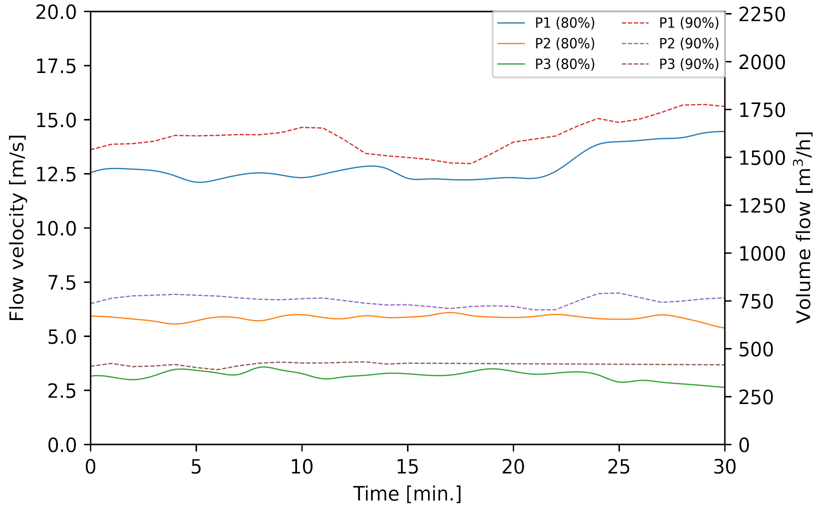

Figure 6: Flow measurements of the TREAS prototype at an ambient temperature and two fan performances. P1, P2 and P3 probing points of the air flow, see Fig. 4.

Table 1: Mean values of the emitted gases.

		CO_2, g	H_2, g	HF, g
Set-up 1	*Average*	215,2	3,0	<0,1
	Std.Dev.	3,0	0,0	—
Set-up 2	*Average*	543,8	5,4	<0,1
	Std.Dev.	90,9	1,3	—
Set-up 3	*Average*	212,7	2,1	<0,1
	Std.Dev.	4,7	0,1	—

The mean emission values were tabulated in Tab. 1. For the first and last set-up with one pouch battery cell, the carbon dioxide values are consistent, together with hydrogen. In second set-up, the amount of carbon dioxide is doubled corresponding to the two pouch cells being burned. Hydrogen concentrations were at the level of 10,000-12,000 ppm v/v, thus not exceeding lower flammability limit (4% v/v for H_2). Carbon dioxide peak value was 4,5% and for the hydrogen was approximately 11000 ppm CO_2 concentration of above 5% may cause already serious effects on human health such as development of hypercapnia and respiratory acidosis [43].

No hydrogen fluoride was recorded for all of the processes. This may be caused due to dilution with high air volume flow (160 l/s). The sole efficiency of dry sorbent injection (without dilution) could not be measured due to excessive temperature of the thermal runaway gases exceeding sensor limits (50°C). Instead the estimated performance of both dry sorbent injection and dilution of the gases for the HF removal is about 99% based on theoretical production of 193.6 mg/Wh [16], and for the CO_2 removal is about 89% based on the theoretical volume of carbon dioxide in pouch NMC cells of 36.6% [44].

Table 2: Maximum temperature rises recorded in testing set-up 1-3 for thermocouple T1-3.

	T1, °C	**T2, °C**	**T3, °C**
Set-up 1 - Tmax	545,3	158,3	100,4
Set-up 2 - Tmax	765,3	186,2	111,3
Set-up 3 - Tmax	756,4	220,7	135,1

Temperature measurement point were positioned above the cell (T1), before the filter (T2) and behind the filter (T3), see Fig. 4. The maximum values recorded in each testing set-up were shown in Tab. 2. The temperature recorded before the filter (158.3-220.7°C) exceeded the maximum temperature allowable for the bag filter (120°C). Bag filter after each testing series was replaced. Despite high volume flow (approx. 1600 m^3/h) and supply of the ambient air, the thermal runaway gas temperature was still relatively high after the filtration.

5 Conclusion

The paper presents the development process of the thermal runaway emissions aftertreatment system. It discusses lithium-ion battery safety concerns in form of thermal runaway, which may happen during the everyday service. During thermal runaway, a plethora of toxic gases is produced, posing significant danger in confined space fire scenarios. Lithium-ion battery fire requires state of art technology to be doused due to its chemical self-sustaining nature. The risk of such fire is minimised with the mandatory testing, that often include causing thermal runaway on purpose. This, however, again is bound to produce vast amounts of toxic substances, which should be filtered or purified.

Following sections characterise potential substances found in TR gas emissions and discusses the compounds in respect to the part of the cell (SEI layer, cathode, anode and electrolyte). The most dangerous compounds for a human found in TR emissions are carbon monoxide and dioxide, hydrogen and hydrogen fluoride. Their toxicity as well as effect on health vary, however all may be categorised as toxic at given concentration levels. Subsequent review of the cleaning methods presents a dry sorbent injection based on calcium hydroxide as a possible solution for the gaseous emissions. The TREAS prototype is developed and subjected to simulation tests, and then a series empirical tests.

Based on the foregoing results, the following conclusions were drawn.

1. Dry sorbent injection based on calcium hydroxide dosage of 1.8 g/s and volume flow of approx. 1600 m^3/h may be used for filtration of the thermal runaway gas emissions with estimated performance of 99% for hydrogen fluoride and 89% for carbon dioxide.

2. Air velocity of 5-7.5 m/s are sufficient to provide dry sorbent transfer and filtration of the emitted gases. Large leakage losses are caused due to sorbent hopper and waste funnel.

3. The average production per Wh for CO_2 and H_2 were 1060,3 mg and 11,8 mg respectively. The peak recorded values were 4,5% (CO_2) and 11000 ppm (H_2).

4. Pouch NCM cell of 220 Wh production of hydrogen did not exceed a lower flammability limit of 40000 ppm v/v.

5. Temperature of the TR gases with the flow level of approx. 1600 m^3/h were at minimum 100,4°C. The temperature of the gas above the burning cells were at maximum 765,3°C.

Acknowledgements

The research was carried out within the fourth edition of the Program of the Polish Ministry of Science and Higher Education entitled ”Doktorat wdrożeniowy” (Industrial Doctoral Program).

Received in June 2023

References

[1] X. Feng, M. Ouyang, X. Liu, L. Lu, Y. Xia, and X. He, “Thermal runaway mechanism of lithium ion battery for electric vehicles: A review,” *Energy Storage Materials*, vol. 10, pp. 246–267, 2018.

[2] M. Ahrens, “Vehicle fires 2020,” report, National Fire Protection Association, 2020.

[3] Deloitte, “2020 global automotive consumer study,” report, Deloitte, 2020. [Online; accessed 14 February 2022].

[4] D. Darnikowski, M. Mieloszyk, and M. Weryk, “Fire resistance of construction elements,” in *Sensors and Smart Structures Technologies for Civil, Mechanical, and Aerospace Systems 2022*, vol. 12046, pp. 203–218, SPIE, 2022.

[5] A. Dorsz and M. Lewandowski, “Analysis of fire hazards associated with the operation of electric vehicles in enclosed structures,” *Energies*, vol. 15, p. 11, Dec 2021.

[6] Y. Chen, Y. Kang, Y. Zhao, L. Wang, J. Liu, Y. Li, Z. Liang, X. He, X. Li, N. Tavajohi, and B. Li, “A review of lithium-ion battery safety concerns: The issues, strategies, and testing standards,” *Journal of Energy Chemistry*, vol. 59, pp. 83–99, 2021.

[7] H. Li, Q. Duan, C. Zhao, Z. Huang, and Q. Wang, “Experimental investigation on the thermal runaway and its propagation in the large format battery module with li (ni1/3co1/3mn1/3) o2 as cathode,” *Journal of hazardous materials*, vol. 375, pp. 241–254, 2019.

[8] Q. Wang, P. Ping, X. Zhao, G. Chu, J. Sun, and C. Chen, “Thermal runaway caused fire and explosion of lithium ion battery,” *Journal of power sources*, vol. 208, pp. 210–224, 2012.

[9] D. Darnikowski, “Fire resistance test methods of battery energy storage systems (bess): analysis, comparison and prospects,” in *Selected Problems in Mechanical Engineering 2022* (M. Mieloszyk and T. Ochrymiuk, eds.), Gdansk, Poland: Wydawnictwo Instytutu Maszyn Przeplywowych PAN, 2022.

[10] A. Börger, J. Mertens, and H. Wenzl, “Thermal runaway and thermal runaway propagation in batteries: What do we talk about?,” *Journal of Energy Storage*, vol. 24, p. 100649, 2019.

[11] M. Ghiji, V. Novozhilov, K. Moinuddin, P. Joseph, I. Burch, B. Suendermann, and G. Gamble, "A review of lithium-ion battery fire suppression," *Energies*, vol. 13, no. 19, 2020.

[12] C. Un and K. Aydın, "Thermal runaway and fire suppression applications for different types of lithium ion batteries," *Vehicles*, vol. 3, no. 3, pp. 480–497, 2021.

[13] S. Ubaldi, C. Di Bari, A. De Rosa, M. Michele, and P. Russo, "Investigation on effective fighting technology for lib fire," *Chemical Engineering Transactions*, vol. 91, pp. 505–510, 2022.

[14] D. Darnikowski and M. Mieloszyk, "Investigation into the lithium-ion battery fire resistance testing procedure for commercial use," *Batteries*, vol. 7, no. 3, p. 44, 2021.

[15] N. Omar, M. Daowd, O. Hegazy, G. Mulder, J.-M. Timmermans, T. Coosemans, P. Van den Bossche, and J. Van Mierlo, "Standardization work for bev and hev applications: Critical appraisal of recent traction battery documents," *Energies*, vol. 5, no. 1, pp. 138–156, 2012.

[16] F. Larsson, P. Andersson, P. Blomqvist, and B.-E. Mellander, "Toxic fluoride gas emissions from lithium-ion battery fires," *Scientific reports*, vol. 7, no. 1, pp. 1–13, 2017.

[17] E. C. for Europe of the United Nations, "Global technical regulation on the electric vehicle safety (evs)," regulation, Mar. 2016.

[18] "Regulation no 100 revision 02 - uniform provisions concerning the approval of vehicles with regard to specific requirements for the electric power train," tech. rep., Economic Commission for Europe of the United Nations, Aug. 2013.

[19] "Regulation no 100 revision 03 - uniform provisions concerning the approval of vehicles with regard to specific requirements for the electric power train," tech. rep., Economic Commission for Europe of the United Nations, Aug. 2021.

[20] "Electrically propelled road vehicles - Test specification for lithium-ion traction battery packs and systems - Part 3: Safety performance requirements," standard, International Organization for Standardization, Geneva, CH, May 2014.

[21] "Electrically propelled road vehicles - Safety specifications - Part 1: Rechargeable energy storage system (RESS)," standard, International Organization for Standardization, Geneva, CH, Apr. 2019.

[22] "Electrically propelled mopeds and motorcycles - Test specifications and safety requirements for lithium-ion battery systems," standard, International Organization for Standardization, Geneva, CH, Apr. 2017.

[23] "Electric and Hybrid Electric Vehicle Rechargeable Energy Storage System (RESS) Safety and Abuse Testing," standard, Society of Automotive Engineers, Warrendale, US, Apr. 2009.

[24] "Lithium-ion traction battery pack and system for electric vehicles - Part 3:Safety requirements and test methods," standard, Standardization Administration of the People's Republic of China, Shenzhen, CN, May 2015.

[25] "Recommended Practices for Abuse Testing Rechargeable Energy Storage Systems (RESSs)," standard, Sandia National Laboratories, Albuquerque, US, July 2017.

[26] "Batteries for Use In Electric Vehicles," standard, Underwriters Laboratories, Northbrook, US, Mar. 2020.

[27] L. Zhao, I. Watanabe, T. Doi, S. Okada, and J. ichi Yamaki, "Tg-ms analysis of solid electrolyte interphase (sei) on graphite negative-electrode in lithium-ion batteries," *Journal of Power Sources*, vol. 161, no. 2, pp. 1275–1280, 2006.

[28] H. Yang, H. Bang, K. Amine, and J. Prakash, "Investigations of the exothermic reactions of natural graphite anode for li-ion batteries during thermal runaway," *Journal of the Electrochemical Society*, vol. 152, no. 1, p. A73, 2004.

[29] G. Gachot, P. Ribière, D. Mathiron, S. Grugeon, M. Armand, J.-B. Leriche, S. Pilard, and S. Laruelle, "Gas chromatography/mass spectrometry as a suitable tool for the li-ion battery electrolyte degradation mechanisms study," *Analytical chemistry*, vol. 83, no. 2, pp. 478–485, 2011.

[30] B. Mao, H. Chen, Z. Cui, T. Wu, and Q. Wang, "Failure mechanism of the lithium ion battery during nail penetration," *International Journal of Heat and Mass Transfer*, vol. 122, pp. 1103–1115, 2018.

[31] X. Feng, X. He, M. Ouyang, L. Lu, P. Wu, C. Kulp, and S. Prasser, "Thermal runaway propagation model for designing a safer battery pack with 25 ah linixcoymnzo2 large format lithium ion battery," *Applied energy*, vol. 154, pp. 74–91, 2015.

[32] H. Arai, M. Tsuda, K. Saito, M. Hayashi, and Y. Sakurai, "Thermal reactions between delithiated lithium nickelate and electrolyte solutions," *Journal of The Electrochemical Society*, vol. 149, no. 4, p. A401, 2002.

[33] J. Li, Z. Zhang, X. Guo, and Y. Yang, "The studies on structural and thermal properties of delithiated lixni1/3co1/3mn1/3o2 (0 ¡ x ? 1) as a cathode material in lithium ion batteries," *Solid State Ionics*, vol. 177, no. 17-18, pp. 1509–1516, 2006.

[34] P. Ping, D. Kong, J. Zhang, R. Wen, and J. Wen, "Characterization of behaviour and hazards of fire and deflagration for high-energy li-ion cells by over-heating," *Journal of Power Sources*, vol. 398, pp. 55–66, 2018.

[35] A. Nedjalkov, J. Meyer, M. Köhring, A. Doering, M. Angelmahr, S. Dahle, A. Sander, A. Fischer, and W. Schade, "Toxic gas emissions from damaged lithium ion batteries - analysis and safety enhancement solution," *Batteries*, vol. 2, no. 1, p. 5, 2016.

[36] V. Somandepalli, K. Marr, and Q. Horn, "Quantification of combustion hazards of thermal runaway failures in lithium-ion batteries," *SAE International Journal of Alternative Powertrains*, vol. 3, no. 1, pp. 98–104, 2014.

[37] A. W. Golubkov, D. Fuchs, J. Wagner, H. Wiltsche, C. Stangl, G. Fauler, G. Voitic, A. Thaler, and V. Hacker, "Thermal-runaway experiments on consumer li-ion batteries with metal-oxide and olivin-type cathodes," *Rsc Advances*, vol. 4, no. 7, pp. 3633–3642, 2014.

[38] A. Dal Pozzo, R. Moricone, A. Tugnoli, and V. Cozzani, "Experimental investigation of the reactivity of sodium bicarbonate toward hydrogen chloride and sulfur dioxide at low temperatures," *Industrial & Engineering Chemistry Research*, vol. 58, no. 16, pp. 6316–6324, 2019.

[39] G. Hunt and M. Sewell, "Utilizing dry sorbent injection technology to improve acid gas control," in *Air and Waste Management Association - International Conference on Thermal Treatment Technologies and Hazardous Waste Combustors*, pp. 144–156, 2015.

[40] Y. Kong and H. Davidson, "Dry sorbent injection of sodium sorbents for so2, hcl and mercury mitigation," in *North American Waste-to-Energy Conference*, vol. 43932, pp. 317–320, 2010.

[41] R. K. Srivastava, W. Jozewicz, and C. Singer, "So2 scrubbing technologies: a review," *Environmental Progress*, vol. 20, no. 4, pp. 219–228, 2001.

[42] D. Schmal, A. Ligtvoet, and A. Brunia, "Some physico-chemical aspects of dry sorbent injection for removal of hci and hf from waste incinerator flue gases," *JAPCA*, vol. 39, no. 1, pp. 55–57, 1989.

[43] P. Parandoush and D. Lin, "A review on additive manufacturing of polymer-fiber composites," *Composite Structures*, vol. 182, pp. 36–53, 2017.

[44] T. Cai, P. Valecha, V. Tran, B. Engle, A. Stefanopoulou, and J. Siegel, "Detection of li-ion battery failure and venting with carbon dioxide sensors," *eTransportation*, vol. 7, p. 100100, 2021.

Analysis of variability and methodology for determining measurement errors in the example of heat recovery systems in air handling units (AHUs)

Robert Matysko*

Institute of Fluid-Flow Machinery, Polish Academy of Sciences
14 Fiszera Street, 80-231, Gdansk, Poland

Abstract

In the paper, a description of the analysis of parameter variability in the studied process is presented, with a focus on the selection of measurement instrument class, using the example of a ventilation system where heat recovery takes place. Additionally, a methodology for determining measurement errors in calculating the heat transfer coefficient from the heat balance equations is provided.

Keywords: Measurement Errors; Measurement Methodology; Heat Transfer Coefficient; Ventilation; Air Conditioning

1 Introduction

In measurements of thermal-fluid parameters, after conducting experimental research, the accuracy of the obtained measurements is determined. The class and range of selected instruments have an impact on the quality and accuracy of the measurements. Knowing the instrument's class and its range allows one to determine the limiting values of measurement errors. However, the choice of a particular measurement instrument is often influenced by its price. In cases where the price is the sole determining criterion for instrument purchase, the quality and accuracy of the measurements may not be satisfactory.

During the design phase of a research setup, calculations of thermal-fluid parameters should be performed. At this stage, the required accuracy of measurement equipment relative to the conducted thermal-fluid process and the requirements for the entire measurement setup can also be determined. Such an analysis enables the specification of instrument ranges and classes and can reduce statistical errors that may arise during data analysis of conducted experiments.

In the literature [1–3] the fundamentals of error analysis in measurement techniques used in engineering are presented. According to [2], measurement uncertainty can be expressed using the estimator of the standard deviation for the mean value [1]. In error analysis, it is crucial to maintain the measurement paths in the appropriate condition,

*Corresponding Author. Email address: matyskor@imp.gda.pl
https://doi.org/10.58139/fn35-m443

which can introduce measurement errors [3]. In the field of thermodynamic measurements, there are numerous instances where experimental research is presented with specified measurement errors [4–6] although the methodology for arriving at the values of these errors for complex quantities is not precisely described mathematically. In this paper, an attempt is made to analyze the variability of technological parameters with regard to the precision of measurements of mathematically complex quantities already during the design phase of the research setup. Mathematical relationships necessary for determining the relative error of the heat transfer coefficient values were also specified.

2 Analysis of Variability in Measurement System Parameters and Instrument Class Selection

This chapter discusses the impact of process variability on the feasibility of obtaining accurate results in experimental research, which is contingent on the choice of measurement equipment. In the conducted analysis, it was assumed that the research subject is a ventilation unit with a heat recovery system. The experimental studies are intended to ascertain heat exchange efficiency and heat transfer coefficient values. To select appropriate measurement devices, a theoretical assessment of the influence of parameter variations, such as dry bulb temperature, volumetric flow rate, relative humidity, and static pressure, on the heat recovery system's efficiency in the ventilation unit was conducted. To effectively balance such a heat recovery system, measurements of these four parameters must be made on both the exhaust and supply sides of the ventilation unit (see Fig. 1). These measurements yield parameters such as mass flow rate, enthalpy of humid air, and heat flow. By conducting an initial analysis of parameter variability, it is possible to determine the type of measurement instrument required to ensure that the measurement of heat recovery efficiency in the ventilation unit is carried out with the necessary precision.

Fig. 1 depicts the reference conditions for the analysis conducted on the influence of individual parameters on the accuracy of the obtained efficiency. Tab. 1 displays the efficiency values obtained under the assumption that only the parameters at the outlet of the ventilation unit on the supply side, which are a result of the heat recovery system's operation, undergo measurement changes.

Tab. 1 provides an example of changes in the calculations of energy efficiency due to small variations in key parameters compared to the reference parameters in Fig. 1. At measurement point number 2, changes were assumed in static pressure at a level of 100 Pa, relative humidity at a level of 0.1%, dry bulb temperature at 0.1°C, and volumetric flow rate at 100 m^3/h. From the obtained calculations, it can be inferred that the accuracy of heat recovery efficiency measurement in the ventilation unit at a 1% level can be compromised if instruments with a wide measurement scale and small elementary division are used. This is particularly noticeable for dry bulb temperature and relative humidity. In this case, if high-precision measurements of energy efficiency are required, it would be advisable to select a temperature sensor with an accuracy of 0.01°C and a humidity transducer with high resolution measuring relative humidity with an accuracy of 0.01 [-]. When setting such high expectations for measurement accuracy, it is also essential to pay attention to the quality of the measurement path and its susceptibility to disturbances (e.g., in the case of voltage measurement signals, cables should be shielded). Maintaining the entire measurement path in the proper condition is crucial, not just the measurement transducers, as a voltage drop of 0.1 V along the path can introduce measurement errors,

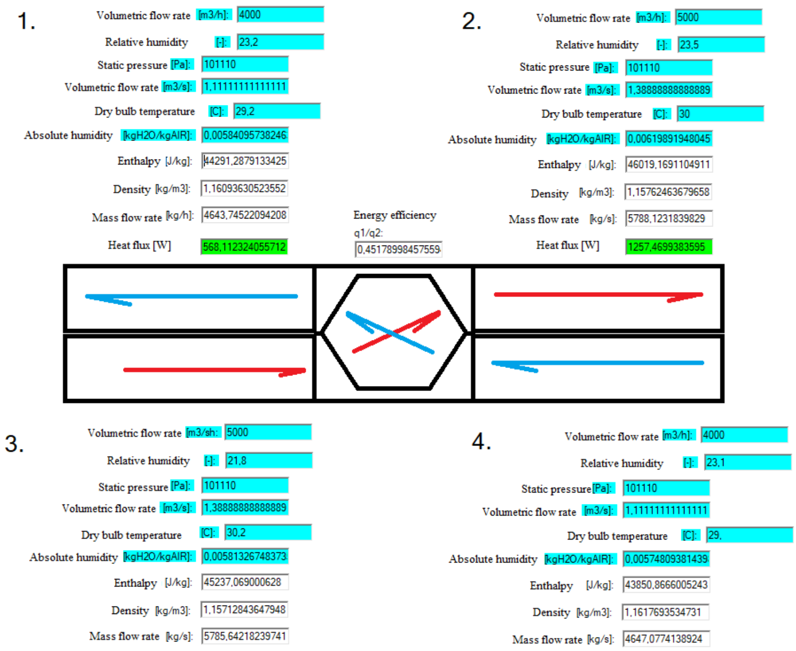

Figure 1: Reference value for impact of variability in AHU efficiency calculations.

which depending on the sensor can significantly disrupt the measurement.

In the context of thermal energy, it is also crucial to ensure high measurement repeatability and precise calibration of individual sensors under uniform test conditions on the ventilation plant.

3 Methodology of Measurement Error Calculations Using the Example of Heat Transfer Coefficient Determination

In this chapter, a methodology for determining measurement errors of the heat transfer coefficient was presented for a ventilation unit operating in conjunction with a heat pump in an intermediate system. The subject of the analysis was the condenser of the heat pump, which served as a heat supply unit for the air supplied from the heat recovery system of the exhaust air. The results of absolute error measurements were presented with respect to the determined value of the heat transfer coefficient and the logarithmic temperature difference. The condensation process involved a mixture of R404A, while water was utilized in the intermediate circuit.

An analysis of errors in the conducted measurements was performed using:

- mathematical statistics methods based on the results of measurement series. This uncertainty is quantified using the standard deviation estimator for the mean, which serves as a numerical measure of the uncertainty referred to as standard uncertainty. When having a series of measurement results, point estimation is used to determine:

Table 1: Analysis of the Impact of Variability in Measured Parameters on the Accuracy of Ventilation Unit Efficiency Measurement

	Reference Values	**Change in Static Pressure**	**Change in Dry Bulb Temperature**	**Change in Volumetric Flow Rate**	**Change in Relative Humidity**
Volumetric Flow Rate [m^3/h]	5000	5000	5000	5100	5000
Relative Humidity [-]	23.5	23.5	23.5	23.5	23.6
Static Pressure [Pa]	101110	101210	101110	101110	101110
Dry Bulb Temperature [°C]	30	30	30.1	30	30
Enthalpy of Humid Air [J/kg]	46019	46003	46212	46019	46087
Density of Humid Air [kg/m^3]	1.157	1.158	1.157	1.157	1.157
Mass Flow Rate [kg/s]	5788	5793	5786	5903	5788
Heat Flow Rate [W]	1257	1233	1568	1282	1366
Efficiency	46%	46%	36%	44%	41%

– the mean value:

$$\bar{x} = \frac{1}{n}\sum_{i=1}^{n} x_i, \tag{1}$$

– the standard uncertainty:

$$u_A = \bar{S}_{\bar{x}} = \sqrt{\frac{1}{n\,(n-1)}\sum_{i=1}^{n}\left(x_i - \bar{x}\right)^2} \tag{2}$$

- data originating from measurement instruments, with the consideration of all available information about factors that might impact the uncertainty of measurement results, along with one's own knowledge and skills acquired through practical measurement experience. When evaluating such uncertainty, only a single measurement value is employed. This value is treated as an estimator of the expected value, with

– the standard uncertainty:

$$u_B = \frac{\Delta_g}{\sqrt{3}}, \tag{3}$$

where Δ_g – the limit value of the error defined by the class indicator, most commonly expressed by the equation:

$$\Delta_g = \frac{Z \cdot K}{100}. \tag{4}$$

In intermediate measurements used to assess the total uncertainty, both of the standard uncertainties mentioned above are employed by computing the combined standard uncertainty:

$$u_ł = \sqrt{u_A^2 + u_B^2}. \tag{5}$$

The standard uncertainty for the mean value is then expressed as follows:

$$u_{\bar{y}} = \sqrt{\sum_{j=1}^{N} \left(\frac{\partial y}{\partial x_j} \cdot u_{ł_j} \right)^2}. \tag{6}$$

Below, the methodology for determining errors in measuring the heat transfer coefficient is presented. In the analysis, the overall uncertainties of the primary quantities utilized in the measurement were taken into account at the following magnitudes:

– Δm_{H_2O}=0.008872 kg/s – error in mass flow rate measurement,

– Δt=0.05°C – error in temperature measurement,

– Δl=0.00002 m – error in the measurement of geometric dimensions of the heat exchanger,

– $\Delta\alpha_{H_2O} = \sqrt{(0.05 \cdot \alpha_{H_2O})^2 + \left(\frac{0.05 \cdot \alpha_{H_2O}}{\sqrt{3}}\right)^2}$ – error in the measurement of the heat transfer coefficient on the water side,

– Δd_{pz}=0.00002 m – error in the inner diameter measurement,

– Δd_{pw}=0.00002 m – error in the outer diameter measurement.

Subsequently, the error in the heat transfer coefficient of the condensation process, which is described by the following equation

$$\alpha_x = \frac{1}{\frac{1}{k_x} - \frac{\frac{d_{pw}}{2}}{\lambda_{cu}} \ln \frac{\frac{d_{pz}}{2}}{\frac{d_{pw}}{2}} - \frac{\frac{d_{pw}}{2}}{\alpha_{H_2O} \cdot \frac{d_{pz}}{2}}}, \tag{7}$$

was determined as

$$\Delta\alpha_x = \sqrt{\begin{aligned} &\left(\frac{\partial\alpha_x}{\partial k_x}\Delta k_x\right)^2 + \left(\frac{\partial\alpha_x}{\partial\lambda_{cu}}\Delta\lambda_{cu}\right)^2 + \left(\frac{\partial\alpha_x}{\partial d_{pw}}\Delta d_{pw}\right)^2 + \\ &\qquad \left(\frac{\partial\alpha_x}{\partial d_{pz}}\Delta d_{pz}\right)^2 + \left(\frac{\partial\alpha_x}{\partial\alpha_{H_2O}}\Delta\alpha_{H_2O}\right)^2 \end{aligned}}. \tag{8}$$

The remaining relationships arise from the law of uncertainty propagation (based on first-order derivatives of the Taylor series) [1]

$$\frac{\partial\alpha_x}{\partial k_x} = \frac{1}{\left(\frac{1}{k_x} - \frac{d_{pw}\ln\left(\frac{d_{pz}}{d_{pw}}\right)}{2\lambda_{cu}} - \frac{d_{pw}}{\alpha_{H_2O} \cdot d_{pz}}\right)^2 \cdot k_z^2}, \tag{9}$$

$$\frac{\partial\alpha_x}{\partial d_{pw}} = -\frac{-\frac{\ln\left(\frac{d_{pz}}{d_{pw}}\right)}{2\lambda_{cu}} + \frac{1}{2\lambda_{cu}} - \frac{1}{\alpha_{H_2O} \cdot d_{pz}}}{\left(\frac{1}{k_x} - \frac{d_{pw}\ln\left(\frac{d_{pz}}{d_{pw}}\right)}{2\lambda_{cu}} - \frac{d_{pw}}{\alpha_{H_2O} \cdot d_{pz}}\right)^2}, \tag{10}$$

$$\frac{\partial \alpha_x}{\partial \lambda_{cu}} = -\frac{d_{pw}\ln\left(\frac{d_{pz}}{d_{pw}}\right)}{2\cdot\left(\frac{1}{k_x} - \frac{d_{pw}\ln\left(\frac{d_{pz}}{d_{pw}}\right)}{2\lambda_{cu}} - \frac{d_{pw}}{\alpha_{H_2O}\cdot d_{pz}}\right)^2 \cdot \lambda_{cu^2}}, \tag{11}$$

$$\frac{\partial \alpha_x}{\partial d_{pz}} = -\frac{-\frac{d_{pw}}{2\lambda_{cu}\cdot d_{pz}} + \frac{d_{pw}}{\alpha_{H_2O}\cdot d_{pz}^2}}{\left(\frac{1}{k_x} - \frac{d_{pw}\ln\left(\frac{d_{pz}}{d_{pw}}\right)}{2\lambda_{cu}} - \frac{d_{pw}}{\alpha_{H_2O}\cdot d_{pz}}\right)^2}, \tag{12}$$

$$\frac{\partial \alpha_x}{\partial \alpha_{H_2O}} = -\frac{d_{pw}}{\left(\frac{1}{k_x} - \frac{d_{pw}\ln\left(\frac{d_{pz}}{d_{pw}}\right)}{2\lambda_{cu}} - \frac{d_{pw}}{\alpha_{H_2O}\cdot d_{pz}}\right)^2 \cdot \alpha_{H_2O}^2 \cdot d_{pz}}. \tag{13}$$

To determine the error of the composite variable k_x

$$k_x = \frac{Q_k}{A_x \Delta t_{\log}}, \tag{14}$$

partial derivatives were calculated for the relationship:

$$\Delta k_x = \sqrt{\left(\frac{\partial k_x}{\partial Q_k}\cdot \Delta Q_k\right)^2 + \left(\frac{\partial k_x}{\partial t_{\log}}\cdot \Delta t_{\log}\right)^2 + \left(\frac{\partial k_x}{\partial A_x}\cdot \Delta A_x\right)^2}, \tag{15}$$

where

$$\frac{\partial k_x}{\partial A_x} = -\frac{Q_k}{A_x^2\cdot \Delta t_{\log}}, \tag{16}$$

$$\frac{\partial k_x}{\partial Q_k} = \frac{1}{A_x\cdot \Delta t_{\log}}, \tag{17}$$

$$\frac{\partial k_x}{\partial \Delta t_{\log}} = -\frac{Q_k}{A_x\cdot \Delta t_{\log}^2}, \tag{18}$$

The error in the determination of the heat exchange surface area:

$$A_x = n\cdot l\cdot d\cdot \pi \tag{19}$$

can be found as

$$\Delta A_x = \sqrt{\left(\frac{\partial A_x}{\partial n}\Delta n\right)^2 + \left(\frac{\partial A_x}{\partial l}\Delta l\right)^2 + \left(\frac{\partial A_x}{\partial d}\Delta d\right)^2}, \tag{20}$$

where

$$\frac{\partial A_x}{\partial n} = l\cdot d\cdot \pi, \tag{21}$$

$$\frac{\partial A_x}{\partial l} = n\cdot d\cdot \pi, \tag{22}$$

$$\frac{\partial A_x}{\partial d} = l\cdot n\cdot \pi. \tag{23}$$

The error in the determination of the logarithmic temperature difference Δ t_{log}:

$$\Delta t_{\log} = \frac{t_1 - t_2}{\ln \frac{t_1}{t_2}} \tag{24}$$

can be found as

$$\Delta\left(\mathit{\Delta} t_{\log}\right) = \sqrt{\left(\frac{\partial\left(\mathit{\Delta} t_{\log}\right)}{\partial t_1}\mathit{\Delta} t_1\right)^2 + \left(\frac{\partial\left(\mathit{\Delta} t_{\log}\right)}{\partial t_2}\mathit{\Delta} t_2\right)^2}, \tag{25}$$

where

$$\frac{\partial\left(\Delta t_{\log}\right)}{\partial t_1} = \frac{1}{\ln \frac{t_1}{t_2}} - \frac{t_1 - t_2}{\ln\left(\frac{t_1}{t_2}\right)^2 t_1}, \tag{26}$$

$$\frac{\partial\left(\Delta t_{\log}\right)}{\partial t_2} = \frac{-1}{\ln \frac{t_1}{t_2}} + \frac{t_1 - t_2}{\ln\left(\frac{t_1}{t_2}\right)^2 t_2}, \tag{27}$$

$$t_1 = t^{wl}_{R404A} - t^{wyl}_{H_2O}\,, \tag{28}$$

$$\mathit{\Delta} t_1 = \sqrt{\left(\frac{\partial t_1}{\partial t^{wl}_{R404A}} \cdot \mathit{\Delta} t^{wl}_{R404A}\right)^2 + \left(\frac{\partial t_1}{\partial t^{wyl}_{H_2O}} \cdot \mathit{\Delta} t^{wyl}_{H_2O}\right)^2}, \tag{29}$$

$$t_2 = t^{wyl}_{R404A} - t^{wl}_{H_2O}\,, \tag{30}$$

$$\mathit{\Delta} t_2 = \sqrt{\left(\frac{\partial t_2}{\partial t^{wyl}_{R404A}} \cdot \mathit{\Delta} t^{wyl}_{R404A}\right)^2 + \left(\frac{\partial t_2}{\partial t^{wl}_{H_2O}} \cdot \mathit{\Delta} t^{wl}_{H_2O}\right)^2}. \tag{31}$$

The heat transfer rate error for the condenser:

$$Q_k = m_{H_2O} \cdot \left(c^{wl}_p \cdot t^{wl}_{H_2O} - c^{wyl}_p \cdot t^{wyl}_{H_2O}\right), \tag{32}$$

can be calculated as

$$\Delta Q_k = \sqrt{\begin{aligned}&\left(\frac{\partial Q_k}{\partial m_{H_2O}}\mathit{\Delta} m_{H_2O}\right)^2 + \left(\frac{\partial Q_k}{\partial c^{wl}_p}\mathit{\Delta} c^{wl}_p\right)^2 + \left(\frac{\partial Q_k}{\partial t^{wl}_{H_2O}}\mathit{\Delta} t^{wl}_{H_2O}\right)^2 \\ &\qquad + \left(\frac{\partial Q_k}{\partial c^{wyl}_p}\mathit{\Delta} c^{wyl}_p\right)^2 + \left(\frac{\partial Q_k}{\partial t^{wyl}_{H_2O}}\mathit{\Delta} t^{wyl}_{H_2O}\right)^2\end{aligned}}, \tag{33}$$

where

$$\frac{\partial Q_k}{\partial m_{H_2O}} = c^{wl}_p \cdot t^{wl}_{H_2O} - c^{wyl}_p \cdot t^{wyl}_{H_2O}\,, \tag{34}$$

$$\frac{\partial Q_k}{\partial c^{wl}_p} = m_{H_2O} \cdot t^{wl}_{H_2O} \tag{35}$$

$$\frac{\partial Q_k}{\partial t_{H_2O}^{wl}} = m_{H_2O} \cdot c_p^{wl}, \tag{36}$$

$$\frac{\partial Q_k}{\partial c_p^{wyl}} = -m_{H_2O} \cdot t_{H_2O}^{wyl}, \tag{37}$$

$$\frac{\partial Q_k}{\partial t_{H_2O}^{wyl}} = m_{H_2O} \cdot c_p^{wyl}. \tag{38}$$

Below in Tab. 2 and Tab. 3 maximum errors determined by the direct and indirect methods are presented, respectively.

Table 2: Summary of Maximum Measurement Errors

Directly Measured Quantities	**Total Standard Uncertainty of Measurement**
Mass Flow Rate $\dot{m}$	$\Delta\dot{m} = \sqrt{0.008^2 \cdot \left(\frac{0.05\cdot\dot{m}}{\sqrt{3}}\right)^2}\ \left[\frac{kg}{s}\right]$
Temperature T	$\Delta T = \sqrt{0.05^2 \cdot \left(\frac{0.05}{\sqrt{3}}\right)^2} = 0.0577°\mathrm{C}$
Inner Pipe Diameter d_{pw}	$\Delta d_{pw} = 0.00002$ m
Outer Pipe Diameter d_{pz}	$\Delta d_{pz} = 0.00002$ m
Heat Transfer Coefficient for Water	$\Delta\alpha_{H_2O} = \sqrt{(0.05 \cdot \alpha_{H_2O})^2 + \left(\frac{0.05\cdot\alpha_{H_2O}}{\sqrt{3}}\right)^2}\ \left[\frac{W}{m^2K}\right]$

Table 3: Summary of Maximum Measurement Errors

Indirectly Measured Quantities	**Maximum Calculated Relative Error**
Heat Transfer Coefficient α_x	$\delta\alpha_x = 0.13$
Overall Heat Transfer Rate k_x	$\delta k_x = 0.07$
Heat flux Q_k	$\delta Q_k = 0.06$

The results of the measurements of the average heat transfer coefficient $\bar{\alpha}$ in the actual condensation zone are presented in Tab. 4, which is an excerpt from the protocol of experimental studies. The maximum deviation of the obtained results for the heat transfer coefficient from the regression line is 29%. The measurement accuracy obtained from experimental studies, which is shown in Fig. 2 and Fig. 3, is related to the measuring apparatus used and the general methodology for determining measurement errors of physically complex quantities and directly results from the class and range of the instruments used and is consistent with the methodology presented in the paper [1].

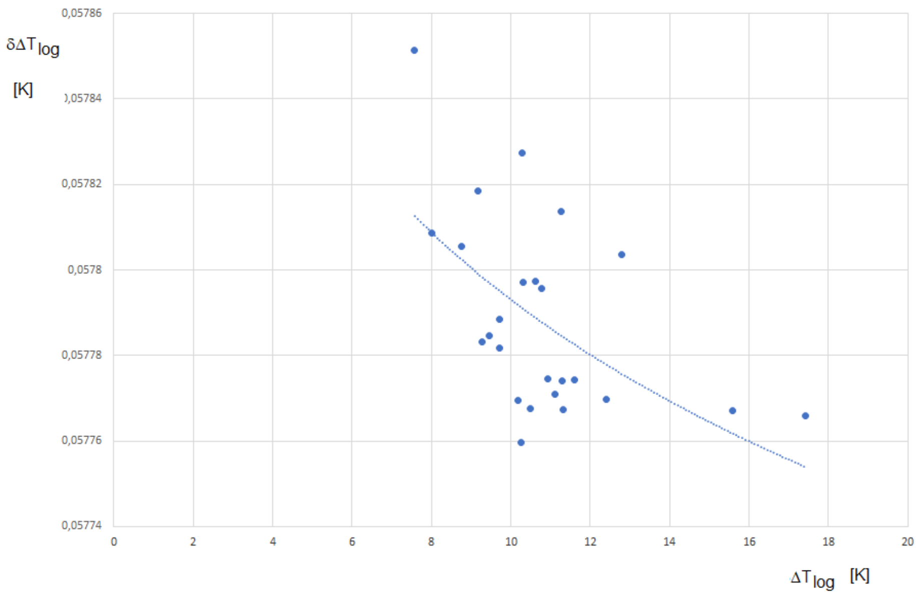

Figure 2: Absolute Measurement Errors for the Measured Logarithmic Temperature Difference.

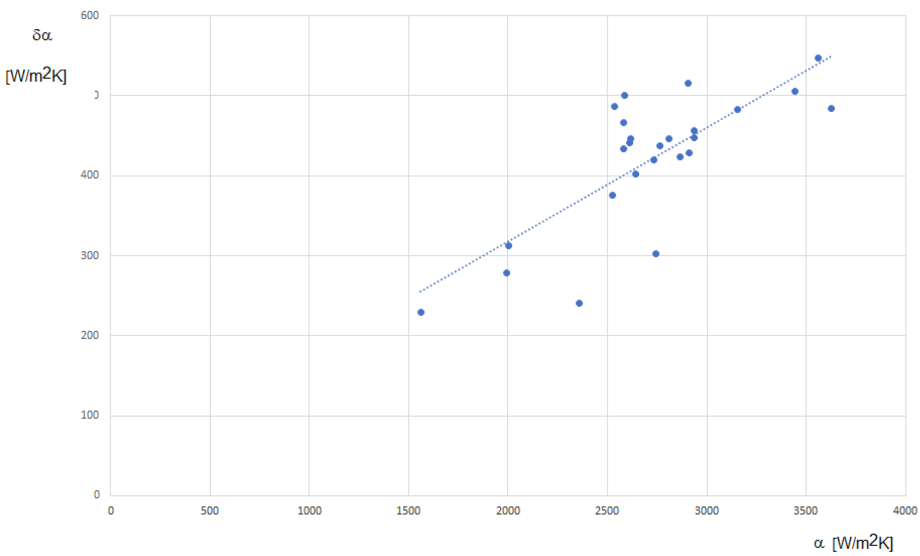

Figure 3: Absolute Measurement Errors for the Measured Heat Transfer Coefficient.

Table 4: Measurement Errors

Measurement number	$\dot{q}$ $\left[\frac{W}{m^2}\right]$	$\mathbf{w}\rho$ $\left[\frac{kg}{m^2 s}\right]$	t_s $[^{\circ}C]$	p_s $[MPa]$	$\bar{\alpha}_{exp}$ $\left[\frac{W}{m^2 K}\right]$	α_{reg} $\left[\frac{W}{m^2 K}\right]$	$\frac{\left(\bar{\alpha}_{exp}-\alpha_{reg}\right)}{\bar{\alpha}_{exp}}$ $[-]$
1	10357	154	26.1	1.31	2074	1983	0.04
2	10436	156	25.6	1.26	2115	1957	0.07
3	14513	161	29.1	1.38	2145	1703	0.21
4	12175	211	27.0	1.35	2652	2007	0.24
5	20367	366	29.5	1.40	4134	2933	0.29
6	18259	418	32.0	1.45	3943	2898	0.26
7	22301	209	35.5	1.65	2198	1722	0.22
8	15862	209	31.0	1.51	2202	1798	0.18
9	12822	198	29.8	1.40	2168	1647	0.24
10	10479	209	28.5	1.34	2287	1880	0.18
11	11870	111	34.6	1.50	1362	1408	-0.03
12	9487	104	29.1	1.40	1295	1378	-0.06
13	12272	215	29.5	1.41	2101	1493	0.29
14	9645	209	28.2	1.35	2073	1540	0.26
15	8717	209	27.0	1.31	2095	1613	0.23
16	13158	115	31.9	1.49	1249	1400	-0.12
17	11683	104	29.6	1.40	1188	1229	-0.03
18	8098	104	26.7	1.31	1196	1252	-0.05
19	7041	104	25.3	1.27	1201	1477	-0.23

where:
$\dot{q}$ – heat flux density given off in the condensation process,
wρ – density of the mass flow rate of the refrigerant,
t_s – condensation temperature of the refrigerant
p_s – condensation pressure of the refrigerant,
$\bar{\alpha}_{exp}$ – average value of the heat transfer coefficient determined based on the experiment,
α_{reg} – average value of the heat transfer coefficient determined from trend line.

From the calculations, the maximum relative error in determining the heat conduction coefficient was obtained δk=7%. Tab. 2 and Tab. 3 present the values of errors obtained through direct and indirect measurement methods, respectively. The maximum relative error in determining the heat transfer coefficient for water was calculated to be 13%. This level of accuracy in determining the heat transfer coefficient for the condensation process was adopted based on the maximum error value obtained from the calculations. In Figs 2 and 3, you can observe the acquired values of errors in logarithmic temperature and heat transfer coefficient (which was presented in Fig. 4). The spread of measurement error results around the trendline is due to the fact that both the logarithmic temperature and heat transfer coefficient are dependent on other measured parameters, which were linked to the experimental research conducted.

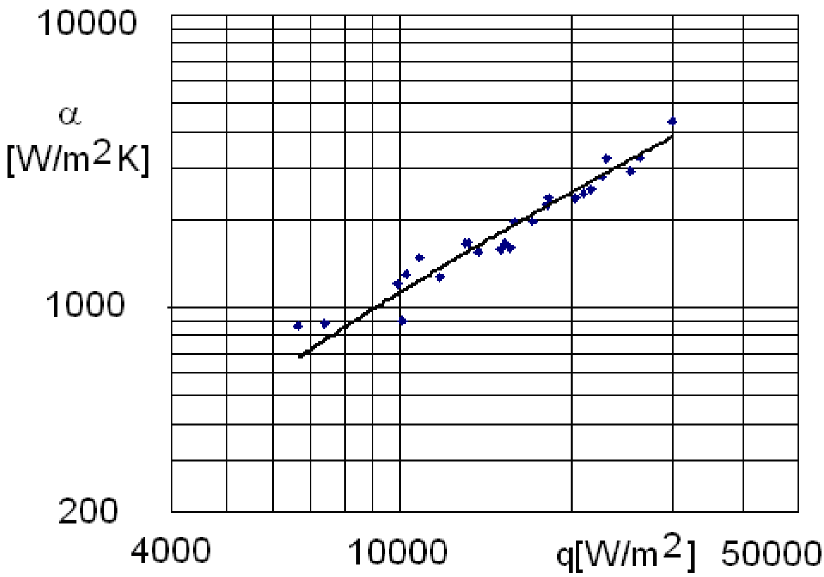

Figure 4: Results of experimental studies of the average value of the heat transfer coefficient.

4 Summary

The provided material presents an analysis of parameter variability in the examined process, taking into account the selection of the measuring instrument class. Additionally, it discusses the methodology for determining measurement errors in thermal-flow measurements practice. The introduction to the work underscores the significance of precise selection of measuring instruments when conducting thermal-flow measurements. An example of a ventilation system with heat recovery is presented as the research object, where measurement accuracy had an impact on determining heat recovery efficiency. While analyzing the variability of parameters such as temperature, flow rate, humidity, and pressure, the authors emphasized the necessity of choosing appropriate class measuring instruments. During the analysis of measurement errors, mathematical statistics methods and information from measuring instruments were utilized. Calculations of errors for the local heat transfer coefficient were also presented as an example. It was pointed out that maintaining measurement paths in the appropriate condition is crucial, as well as ensuring measurement repeatability and precise sensor calibration. In conclusion, the analysis of parameter variability and the precision of measuring instruments are crucial for obtaining reliable results in thermal-flow measurements. Simultaneously, the methodology for assessing measurement errors plays a significant role in ensuring measurement accuracy in practice.

Received in November 2023

References

[1] J. R. Taylor and W. Thompson, *An introduction to error analysis: the study of uncertainties in physical measurements*, vol. 2. Springer, 1982.

[2] ISO/IEC Guide 98-3:2008, "Guide to the expression of uncertainty in measurement," *International Organization for Standardization.*

[3] P. Bevington and D. Robinson, *Data Reduction and Error Analysis for the Physical Sciences. 2nd ed.* New York: McGraw-Hill, 1992.

[4] M. Jaremkiewicz, "Reduction of dynamic error in measurements of transient fluid temperature," *Archives of Thermodynamics*, vol. 32, no. 4, pp. 55–66, 2011.

[5] J. Taler, D. Taler, T. Sobota, and P. Dzierwa, "New technique of the local heat flux measurement in combustion chambers of steam boilers," *Archives of Thermodynamics*, vol. 32, no. 3, pp. 103–116, 2011.

[6] M. Szega and G. T. Nowak, "Identification of unmeasured variables in the set of model constraints of the data reconciliation in a power unit," *Archives of thermodynamics*, vol. 34, no. 4, pp. 235–245, 2013.

Notes for Contributors

TRANSACTIONS OF THE INSTITUTE OF FLUID-FLOW MACHINERY publishes original papers which have not previously appeared in other journals. The journal does not have article processing charges (APCs) nor article submission charges. The language of the papers is English. The paper should not exceed the length of 20 pages. All pages should be numbered. The plan and form of the papers should be as follows:

1. The heading should specify the title (as short as possible), author, his/her complete affiliation, town, zip code, country. Please indicate the corresponding author and his/her e-mail address. The heading should be followed by *Abstract* of maximum 15 typewritten lines and *Keywords*.
2. More important symbols used in the paper can be listed in *Nomenclature*, placed below *Abstract* and arranged in a column, e.g.:
   u – velocity, m/s
   v – specific volume, m/kg
   etc.
   The list should begin with Latin symbols in alphabetical order followed by Greek symbols also in alphabetical order and with a separate heading. Subscripts and superscripts should follow Greek symbols and should be identified with separate headings. Physical quantities should expressed in SI units (*Système International d'Unités*).
3. All abbreviations should be spelled out the first time they are introduced in text.
4. The equations should be each in a separate line. Standard mathematical notation should be used. All symbols used in equations must be clearly defined. The numbers of the equations should run consecutively, irrespective of the division of the paper into sections. The numbers should be given in round brackets on the right-hand side of the page.
5. Particular attention should be paid to the differentiation between capital and small letters. If there is a risk of confusion, the symbols should be explained (for example *small c*) in the margins. Indices of more than one level (such as B_{f_a}) should be avoided wherever possible.
6. Computer-generated figures should be produced using **bold lines and characters**. No remarks should be written directly on the figures, except numerals or letter symbols only. The relevant explanations can be given below in the caption.
7. The figures, including photographs, diagrams, etc., should be numbered with Arabic numerals in the same order in which they appear in the text. Each figure should have its own caption explaining the content without reference to the text.
8. Computer files on an enclosed disc or sent by e-mail to the Editorial Office are welcome. The manuscript should be written as a MS Word file – $*$*.doc*, $*$*.docx* or LaTeX file – $*$*.tex*. For revised manuscripts after peer review, figures should be submitted as separate graphic files in either vector formats (PostScript (PS), Encapsulated PostScript (EPS), preferable, CorelDraw (CDR), etc.) or bitmap formats (Tagged Image File Format (TIFF), Joint Photographic Experts Group (JPEG), etc.), with the resolution not lower than 300 dpi, preferably 600 dpi. These resolutions refer to images sized at dimensions comparable to those of figures in the print journal. Therefore, electronic figures should be sized to fit on single printed page and can have maximum 120 mm x 170 mm. Figures created in MS World, Exel, or PowerPoint will not be accepted. The quality of images downloaded from websites and the Internet are also not acceptable, because of their low resolution (usually only 72 dpi), inadequate for print reproduction.

9. The references for the paper should be numbered in the order in which they are called in the text. Calling the references is by giving the appropriate numbers in square brackets. The references should be listed with the following information provided: the author's surname and the initials of his/her names, the complete title of the work (in English translation) and, in addition:

   (a) for books: the publishing house and the place and year of publication, for example: [1] `Holman J.P.:` *Heat Transfer*. `McGraw-Hill, New York 1968.`

   (b) for journals: the name of the journal, volume (Arabic numerals in bold), year of publication (in round brackets), number and, if appropriate, numbers of relevant pages, for example:
   `[2] Rizzo F.I., Shippy D.I.:` *A method of solution for certain problems of heat conduction*. `AIAA J.` **8** `(1970), No. 11, 2004-2009.`

   For works originally published in a language other than English, the language should be indicated in parentheses at the end of the reference.

   Authors are responsible for ensuring that the information in each reference is complete and accurate.

10. As the papers are published in English, the authors who are not native speakers of English are obliged to have the paper thoroughly reviewed language-wise before submitting for publication.

Manuscript submission Manuscript should be mailed to the Transactions of the Institute of Fluid-Flow Machinery Editorial Office (Wydawnictwo IMP PAN) at the Institute of Fluid-Flow Machinery PAS, Fiszera 14, 80-231 Gdańsk, Poland, or (electronicaly) sent as e-mail attachment to the Editorial Office at redakcja@imp.gda.pl. Three hard copies of the manuscript including figures, photographs, diagrams and tables should be submitted simultaneously with the electronic copy. Manuscript submitted only electronically (document or source file) must be supplied with its PDF file.

The illustrations may be submitted in color, however they will be printed in black and white in the journal, so the grayscale contributions are preferable. Therefore, the figure caption and the entire text of the paper should not make any reference to color in the illustration. Moreover the illustration should effectively convey author's intended meaning when it is printed as a halftone. The illustrations will be reproduced in color in the online publication.

Further information All manuscripts will undergo some editorial modification. The paper proofs (as PDF file) will be sent by e-mail to the corresponding author for acceptance, and should be returned within two weeks of receipt. Within the proofs corrections of minor and typographical errors in: author names, affiliations, articles titles, abstracts and keywords, formulas, symbols, grammatical error, details in figures, etc., are only allowed, as well as necessary small additions. The changes within the text will be accepted in case of serious errors, for example with regard to scientific accuracy, or if authors reputation and that of the journal would be affected. Submitted material will not be returned to the author, unless specifically requested.

A PDF file of published paper will be supplied free of charge to the Corresponding Author.

Submission of the manuscript expresses at the same time the authors consent to its publishing in both printed and electronic versions.

Transfer of Copyright Agreement Submission of the manuscript means that the authors automatically agree to assign the copyright to the Publisher. Once a paper has been accepted for publication, as a condition of publication, the authors are asked to send by email a scanned copy of the signed original of the Transfer of Copyright Agreement, signed by the Corresponding Author on behalf of all authors to the Managing Editor of the Journal. The copyright form can be downloaded from the journal's website at http://www.imp.gda.pl/transactions-of-iffm/ under Notes for Contributors.

CONTENTS

ISSN 0079–3205